

Chapter 4

3D Field Data Test

In this chapter, I test the rock physics constrained anisotropic WEMVA methodology on a 3-D Gulf of Mexico dataset. Based on the well logs and the previously inverted lithological interpretations, I perform stochastic rock physics modeling to sample the possible ranges of the anisotropic parameters. These modeling results are then summarized by an average model and a cross-parameter covariance matrix under the multivariate Gaussian assumption. When inverting the surface seismic data using the anisotropic WEMVA method, I start from the average model and regularize the inversion using the geological dips and the cross-parameter covariance. The inverted VTI model simultaneously explains the surface seismic data (minimizes the anisotropic WEMVA objective function), follows the geological structures, and is consistent with the rock physics principles. The migration image based on the inverted models shows higher resolution and clear definition of the dipping sedimentary layers around the salt in the shallow region. The improved VTI model also yields a better focused image at depth.

INTRODUCTION

Earth model building is an underdetermined and hence challenging inverse problem, especially at the exploration stage. In general, the input information can be obtained

from geological information, surface seismic data, and well log measurements (Woodward et al., 2014). Surface seismic data have the best compromise between accuracy and coverage among the three types of information. Geological knowledge covers large regions, whereas well logs provide accurate high resolution information only at sparse locations. Therefore, most of the current information integration practices occur after seismic imaging and structural interpretation. First, seismic images are stretched vertically according to the well markers. Then, borehole analysis is extrapolated from the well location to the rest of the region based on the seismic images and the underlying geological assumptions. This conventional workflow does not include a feedback loop to verify if the modified seismic images honor the kinematics of the seismic data. Therefore, inconsistencies may be introduced by the sequential evaluations of the data.

In this chapter, I examine a surface seismic dataset that was acquired offshore Gulf of Mexico (GoM) by Schlumberger Multiclient. Migration images based on isotropic Earth models are obtained from the seismic data and the reservoir properties are interpreted based on the well logs following a conventional data integration workflow. However, both the well logs and the lithological interpretations suggest that the sedimentary basin consists of large portion of shales, which contradicts the isotropic Earth assumption used in seismic imaging. Furthermore, the migration image manifests steep dips in both in-line and cross-line directions where the sediments were pushed up by salt intrusion. Wavepaths reflected from these structures can be highly sensitive to the anisotropic parameters. Consequently, the inconsistencies in the isotropic Earth model may lead to defocused image and/or incorrect positioning of the reflectors.

To take advantage of the complementary information in all data, I propose to integrate geological and rock physics information during the seismic inversion when building an anisotropic Earth model. As introduced in the previous chapter, I include the geological information as dip filters and rock physics information as cross-parameter covariances (Li et al., 2011; Woodward et al., 2014; Zdraveva et al., 2014). By evaluating all objectives simultaneously, I hope to resolve anisotropic Earth models that

are consistent with all the available data.

Another challenge of the field application is the computational cost associated with the large volume of data. To overcome this difficulty, various data reduction methods have been proposed. Whitmore (1995); Shen and Symes (2008) and Tang et al. (2008) proposed to assemble point sources into a smaller number of plane-wave sources. However, this strategy leaves artifacts in the model space which can translate into false model updates by certain sensitive WEMVA objective functions. Guerra et al. (2009) proposed to select isolated image points in the subsurface to create a smaller dataset and evaluate the accuracy of the model in a certain targeted area. However, the resolution of this method is limited by the density of the selected image points. Large number of densely sampled image points with corresponding subsurface gathers are needed for higher resolution, which increases the computational cost. Tang and Biondi (2011) proposed to model a smaller dataset using the Born modeling method with the prestack subsurface offset domain common image gathers to maintain the velocity information in the original dataset. This method is effective in reducing the data size and hence the computational cost when the target area is significantly smaller than the original study area. It assumes a correct velocity model above the target area. At the exploration stage, a reliable anisotropic model is needed for the whole area and the initial model is often far from accurate (isotropic vs. anisotropic). Therefore, this target-oriented method cannot be applied. Instead, I take advantage of the redundancy of the data when computing the gradient by randomly removing two thirds of all shots in each iteration (Friedlander and Schmidt, 2012). We show that the gradients obtained by the reduced number of shots contain the same update information with limited under-stacked noise and unbalance amplitude effects. These artifacts can be suppressed by changing the random set of shots through WEMVA iterations.

This chapter contains two parts. In the first part, I perform stochastic rock physics modeling based on the well log measurements and the interpretation results output from a previous seismic processing workflow. This exercise enables us to explore the possible range of the anisotropic models. I obtain the background (averaged)

anisotropic model to initialize the WEMVA inversion and the cross-parameter covariance matrix to regularize the inversion.

In the second part, I invert a subset of the 3-D GoM seismic data set based on the model and the constraints from the stochastic rock physics modeling. Inversion results show improvements with higher resolution and better definition of the sedimentary structure around the salt.

STOCHASTIC ROCK PHYSICS MODELING FOR SHALE ANISOTROPY

Many rock physics models have been proposed to describe shale anisotropy, considering both the intrinsic mineral anisotropy and the particle alignment during compaction. In this thesis, I combine the rock physics models proposed by Bachrach (2010a) and Bandyopadhyay (2009). I model a sedimentary rock using two distinctive rock components: the anisotropic shale and the isotropic sand. Shale anisotropy comes from three aspects: intrinsic anisotropy from smectite and illite, the compaction effect on the mineral alignment, and the transition from smectite to illite due to compaction and temperature. I model the sand using pure quartz, which is assumed isotropic. To combine the sand component with the shale component, I consider two effective medium models: the suspension model and the lamination model. In the suspension model, sand (quartz) is modeled as inclusions in the anisotropic shale background. In the lamination model, sand and shale are modeled as a laminated system.

Details of the rock physics modeling are presented in Appendix B. I summarize the process of anisotropic rock physics modeling in Algorithm 2. To model the rock physics properties, models for earth temperature, porosity and shale percentage are needed. I estimate these models from both well logs and previous lithological inversion results. A few key parameters are also needed. These parameters are highly uncertain even with well log measurements. Therefore, I capture the uncertainties in these parameters by randomly sampling a uniform distribution for each parameter at each

rock physics realization. The ranges of the uniform distribution for each parameter are determined based on the previous studies.

By varying the key parameters of the rock physics model, I explore different shale rock scenarios with varying initial compaction states, compaction rates, temperature gradients, and temperature windows for smectite-to-illite transition. As a result, I capture the uncertainties in the rock physics modeling and obtain an ensemble of models instead of a single model. These models are the sources of the prior rock physics knowledge.

Algorithm 2 Stochastic rock physics modeling workflow

```

for  $n = 1 \cdots N_{\text{real}}$  do
  Initialize the modeling parameters.
  Compute the percentage of illite in the rock given a temperature model.
  Compute the average stiffness coefficients for smectite and illite, given a porosity model.
  Compute the volumetric percentage for each of the mineral phase, given a volumetric percentage of shale.
  Compute the effective stiffness coefficients using suspension model and lamination model.
  Compute the VTI models from the effective stiffness coefficients.
end for

```

Figure 4.1(a) shows the input models for the rock physics modeling. I derive the shale content from gamma ray measurements by a simple linear stretch. I filter out the high frequencies of these models since they are beyond the seismic resolution. Figure 4.1(b) shows two instances of the modeling results. The first and third panels in Figure 4.1(b) show the ϵ and δ models using the lamination model. The second and fourth panels in Figure 4.1(b) show the ϵ and δ models using the inclusion model. In general, anisotropic parameters predicted by both models correlate with the shale content in the well log. We observe that different rock physics models produce greater differences in δ model than in ϵ model.

Besides the well log measurements, an initial isotropic processing work flow has been applied on the field data by Schlumberger. Seismic inversion results, such as, P-wave velocity, shale content, and porosity are provided. The comparison between the

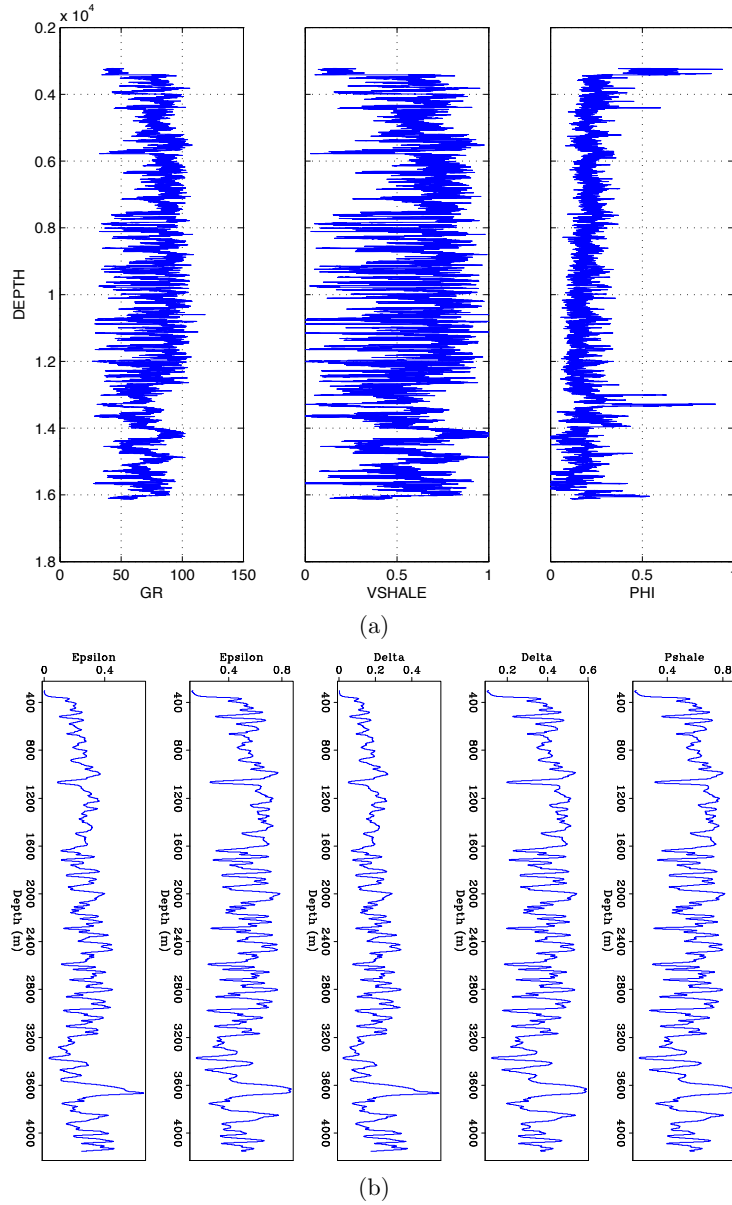


Figure 4.1: (a): Input of the rock physics modeling from well log measurements. From left to right: gamma ray measurements, deduced shale contents from gamma ray and porosity measurements. (b): One instance of the rock physics modeling experiment. From left to right, panels are ϵ profile from the lamination model and inclusion model; δ profile from the lamination model and inclusion model; shale content at the well location. [ER] `chap4/. wellinput,cmpmodel`

porosity inversion result and the well log measurements at the well location suggests that the porosity inversion from seismic is unreliable. The unreliability is probably due to the lack of low frequencies in the seismic data. However, the inversion result for shale content is comparable to the well log measurements. Therefore, I use the provided shale content inversion cube (Figure 4.2(a)) but model a smoothly varying porosity trend (Figure 4.2(b)) from the provided P-wave velocity. The high shale content estimates indicate that the subsurface is rich in clay minerals at all depths, although the shale content slightly increases with depth. The low porosity region below 5 km in Figure 4.2(b) highlights a shale-rich basin. The resolution of the shale content corresponds to a much larger scale (order of tens of meters) than the inclusion rock model (order of centimeters). Therefore, I use the lamination model to estimate the shale anisotropy.

Using the input in the three-dimensional space, I am able to model the anisotropic parameters in 3-D based on the rock physics models. Figure 4.2(c) and Figure 4.2(d) show an example of the ϵ and δ model. The maximum resolution of the modeled elastic constants is similar to the resolution of the interpreted shale content. Nonetheless, users can control the resolution of the anisotropic models by smoothing the modeling results. Given the chosen rock physics model, both anisotropic parameters ϵ and δ are correlated with the shale content and are inversely correlated with the porosity.

More importantly than producing a single modeling result, the stochastic rock physics modeling also allows us to explore the possible ranges of the anisotropic parameters. At a particular location in the subsurface, I obtain an ensemble of vertical velocity, ϵ , and δ values while sampling the distribution of the key parameters, as shown in Figure 4.3. Assuming the three parameters v_v , ϵ , and δ follow a multi-variant Gaussian distribution, I summarize their variance with a 3×3 matrix with 6 independent elements. This cross-covariance matrix is estimated at each subsurface location.

Figures 4.4(a) to 4.4(c) show the diagonal elements in the covariance matrix. The strong lateral variations in vertical velocity variance (Figure 4.4(a)) and in ϵ variance show that their uncertainties are strongly correlated with the lithology. The

δ variance (Figure 4.4(c)) show less lateral variations, indicating that parameter δ is mainly controlled by compaction and mineral transition.

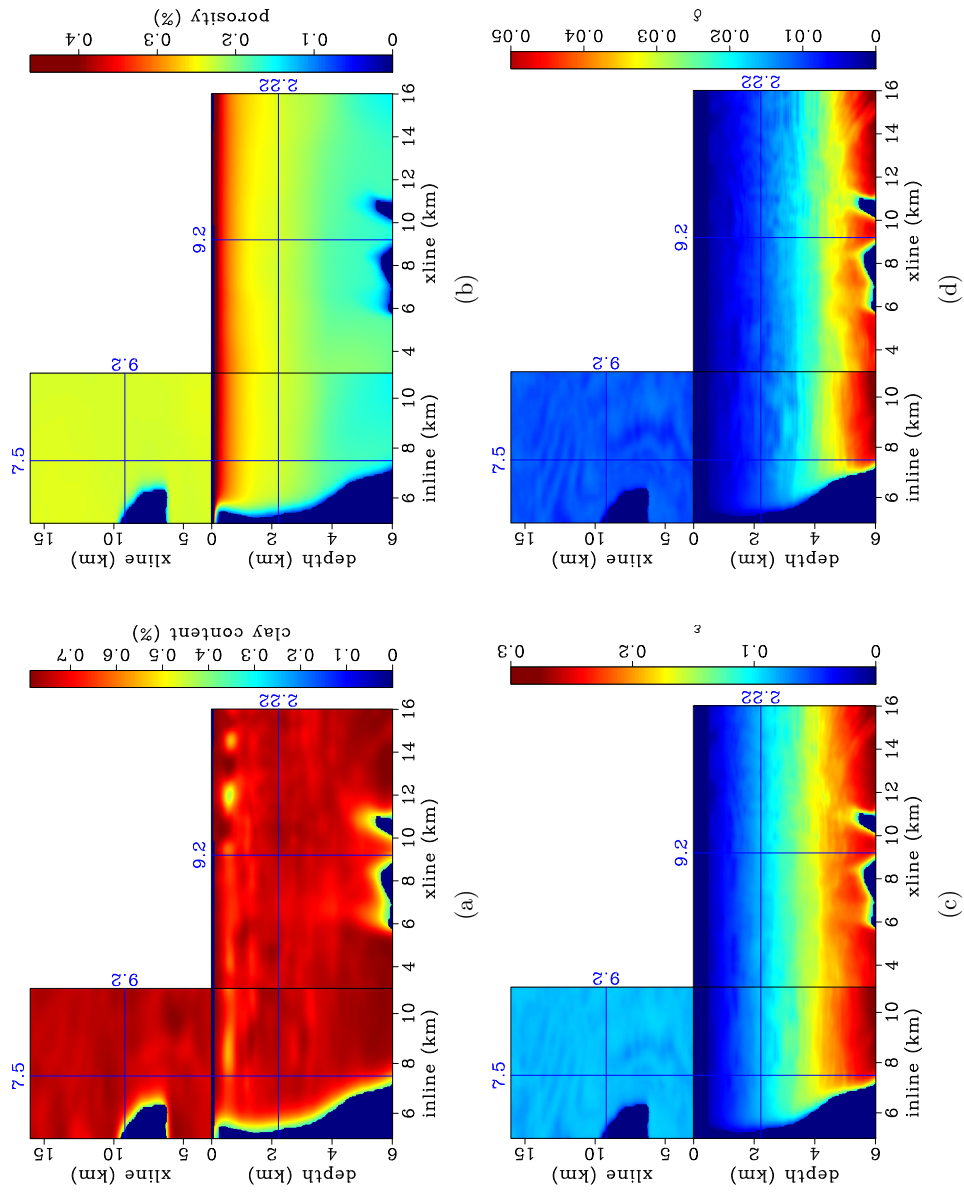


Figure 4.2: Interpreted shale content (a) and modeled porosity (b). Average ϵ model (c) and average δ model (d). Both models are obtained from the stochastic rock physics modeling experiment. [ER]

chap4/. peltrend,phitrend,epstrend,deltrend

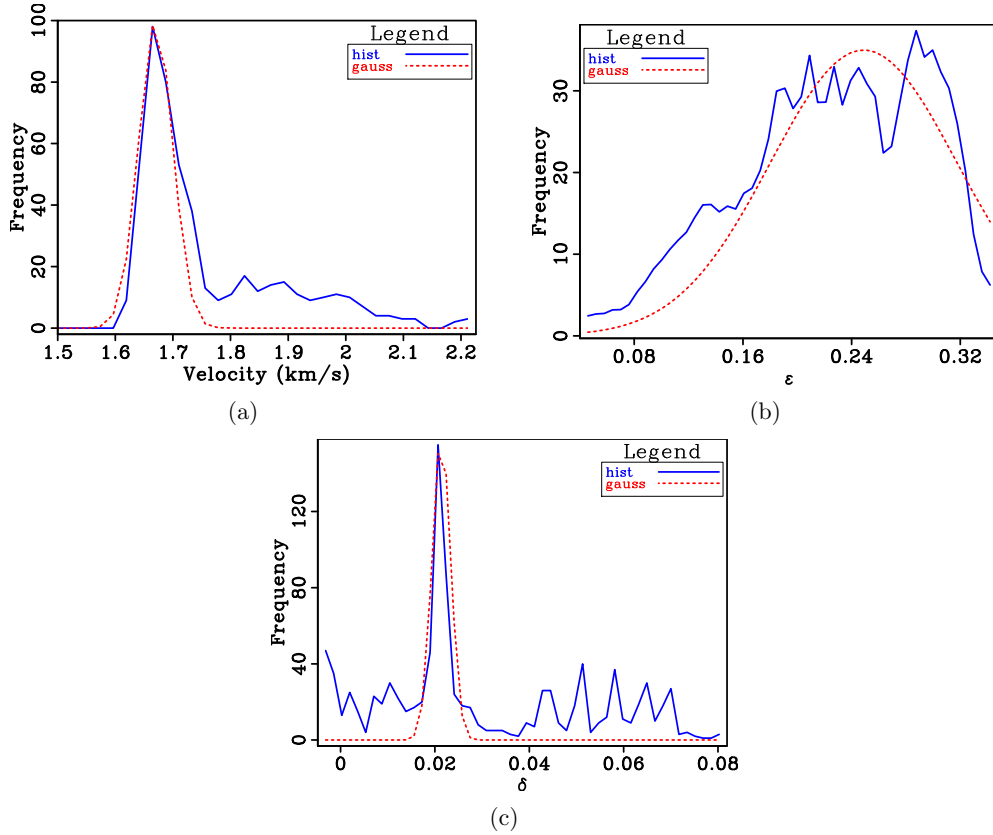


Figure 4.3: Stochastic rock physics modeling results for (a) vertical velocity; (b) ϵ ; and (c) δ . The solid line in each panel denotes the numerical histogram for each model variable. The dashed line denotes the approximated multivariate Gaussian distribution based on the numerical realizations. [ER] chap4/. vp0hist,epshist,delhist

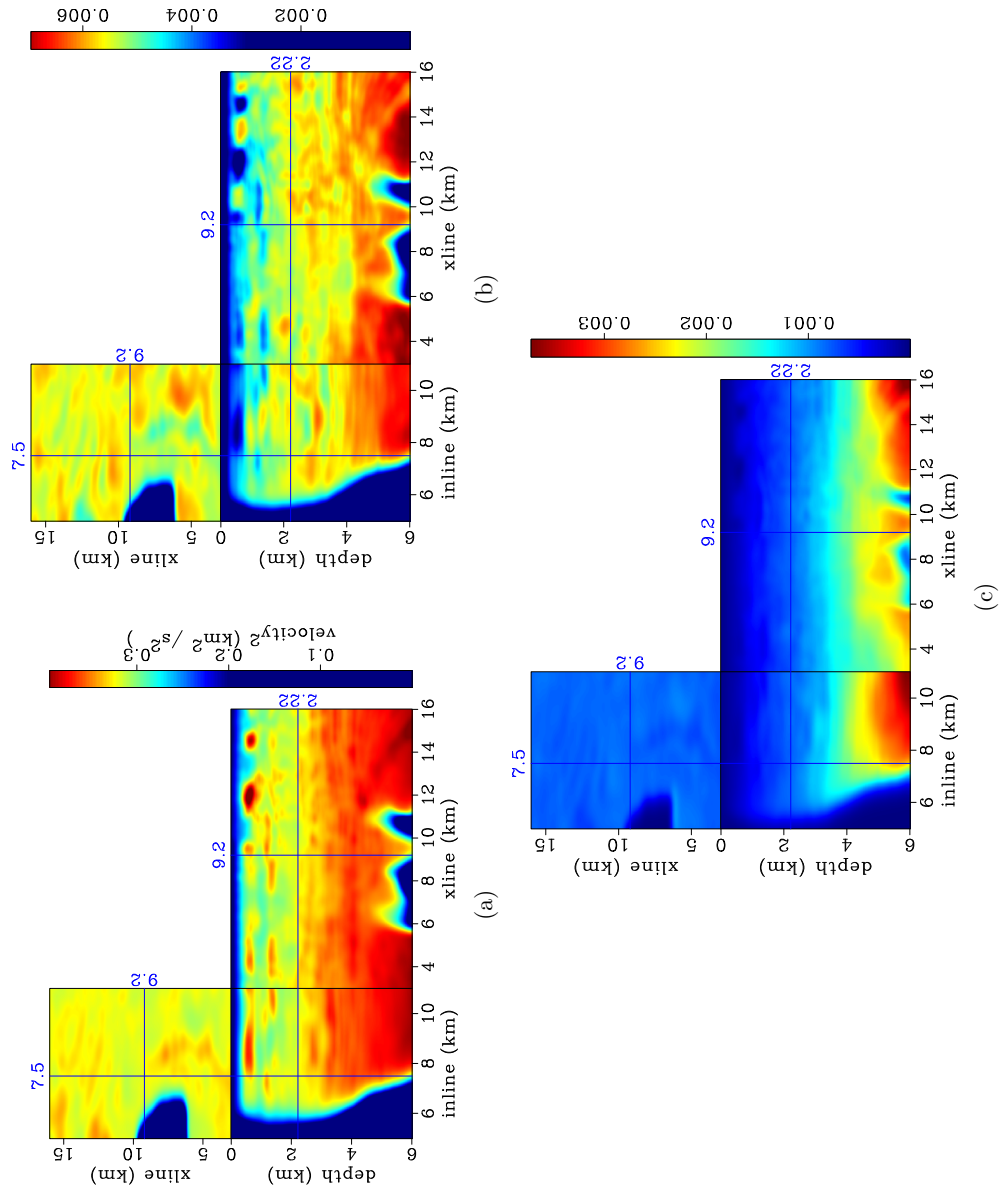


Figure 4.4: Diagonal elements of the covariance matrix. (a): Variance of vertical velocity; (b): Variance of ϵ ; and (c): Variance of δ . [ER] chap4/. covancvv,covancee,covancedd

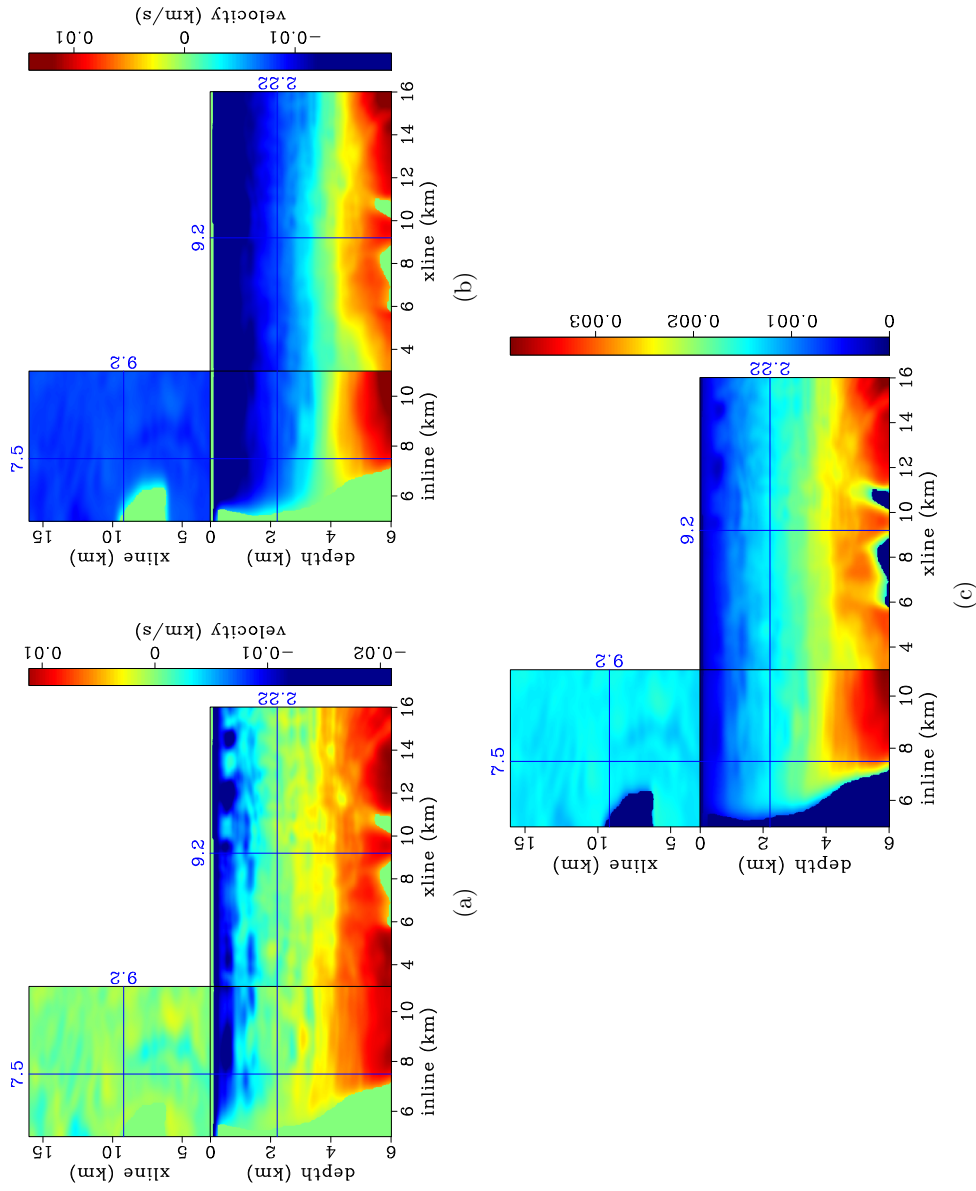


Figure 4.5: Off-diagonal elements of the covariance matrix. (a): Covariance between vertical velocity and ϵ ; (b): Covariance between vertical velocity and δ ; and (c): Covariance between ϵ and δ . [ER]

chap4/. covancve,covancvd,covanced

Figures 4.5(a) to 4.5(c) show the off-diagonal elements in the covariance matrix. The cross-covariances between v_0 and ϵ (Figure 4.5(a)) as well as between v_0 and δ suggest that velocity and anisotropy are negatively correlated in the shallow region but positively correlated in the deep region. This correlation can be explained by rock properties. In the shallow region, high velocity correlates with low anisotropic sand; whereas in the deeper region, high velocity can be caused by mineral diagenesis from smectite to illite, which is also highly anisotropic (Vernik and Liu, 1997). Covariance between ϵ and δ (Figure 4.5(c)) shows positive correlations for all depths.

ANISOTROPIC WEMVA ON 3-D FIELD DATA IN THE GULF OF MEXICO

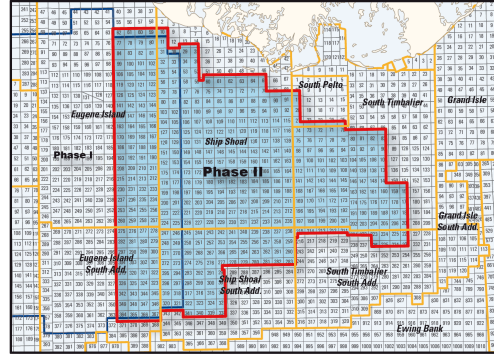
The most important piece of information of the subsurface comes from the seismic data. In this section, I discuss the preprocessing and the inversion of the seismic data to build reliable anisotropic models.

Acquisition and preprocessing

The data were acquired offshore Louisiana in the Gulf of Mexico. Figure 4.6 plots the region that the acquisition covered. Both the pressure and the vertical displacement were measured using sensors laid out along ocean bottom cables (OBC). I was provided with the P-Z summed data in which only the up-going wavefield was retained.

I work with a subset of the 3-D dataset due to the limited computational resources. Figure 4.7 shows the source and receiver locations of the study area given by the acquisition. The source lines are orthogonal to the receiver cables to produce an even midpoint fold. The sources are spaced 400 m in-line and 50 m cross-line (with respect to the receiver lines). The receivers are spaced 50 m in-line and 600 m cross-line. Due to the relatively sparse receiver locations, I use reciprocity to exchange the sources and receivers in the migration.

Figure 4.6: Area covered by the E-Dragon Phase II acquisition. Ocean bottom cables were laid out on the sea bed under shallow water with an average depth of 120 m. [NR] chap4/. dragonarea



I group the receivers onto a 50 m×600 m grid and the sources onto a 50 m×50 m grid. Figure 4.8 shows the acquisition pattern for a single receiver, and Figure 4.9 shows the corresponding receiver gather. In the in-line direction, large acquisition holes are consistent with the sparse in-line source sampling. In the better sampled cross-line direction, I notice strong dispersive arrivals with high amplitudes after 3.5 s. These low frequency surface wave events dominate the receiver gathers in the later time.

To remove the surface waves, I apply a bandpass filter to select the reflection energy between 3 Hz and 25 Hz. The upper bound of the frequency band is limited by the available computational resources. I also apply a first arrival muting and a $t^{2.5}$ time weighting on the receiver gather to boost up the later arrivals. The receiver gather after preprocessing is shown in Figure 4.10. I regard the receiver gather as a shot gather and use the implicit finite different implementation of the VTI one-way wave-equation (Shan, 2008) to perform shot-profile migration.

Initial anisotropic models and gradients

An initial ray-based tomography has been performed by Schlumberger MultiClient. Figure 4.11(a) shows the provided isotropic velocity model. Figures 4.11(b) to 4.11(d) show the initial anisotropic model. The initial ϵ model (Figure 4.11(c)) and δ model (Figure 4.11(d)) are the averaged models from the stochastic rock physics modeling.

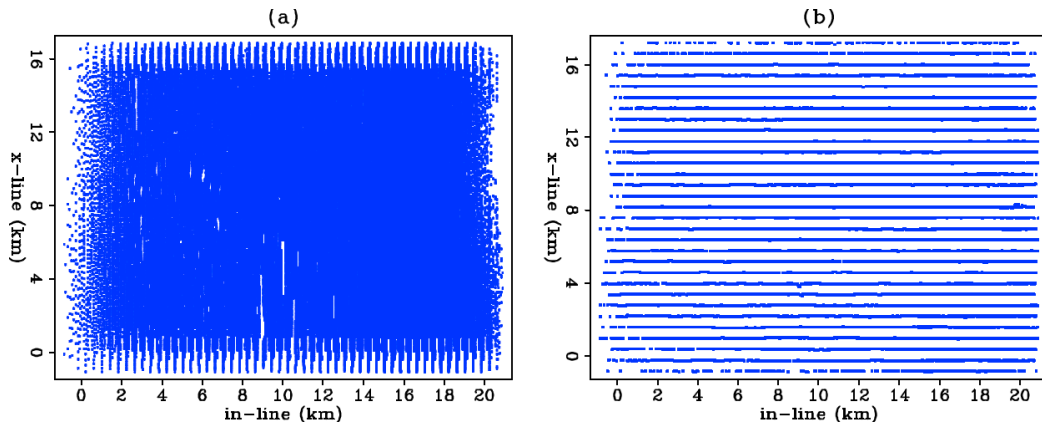
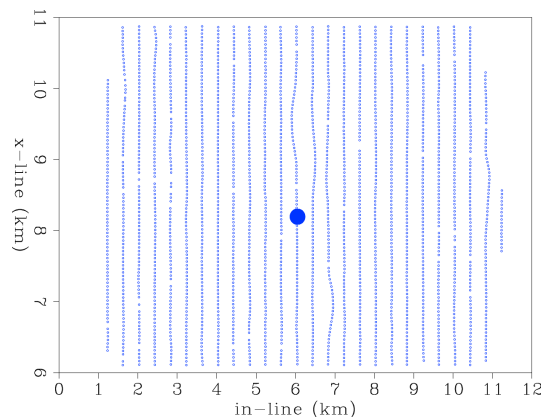


Figure 4.7: Cross-spread geometry of the GoM dataset. Panel (a): Source locations; Panel (b): Receiver locations. The source lines and the receiver lines are perpendicular to each other. I define the direction along the receiver lines the in-line direction and the perpendicular direction cross-line direction. [ER] chap4/. patch-geo

Figure 4.8: Acquisition pattern for one particular receiver. Source locations are denoted by "o" and the receiver location is denoted as the solid circle. For any given receiver, the maximum in-line offset is about 6 km and the maximum cross-line offset is about 3 km. [ER] chap4/. 1rec-geo



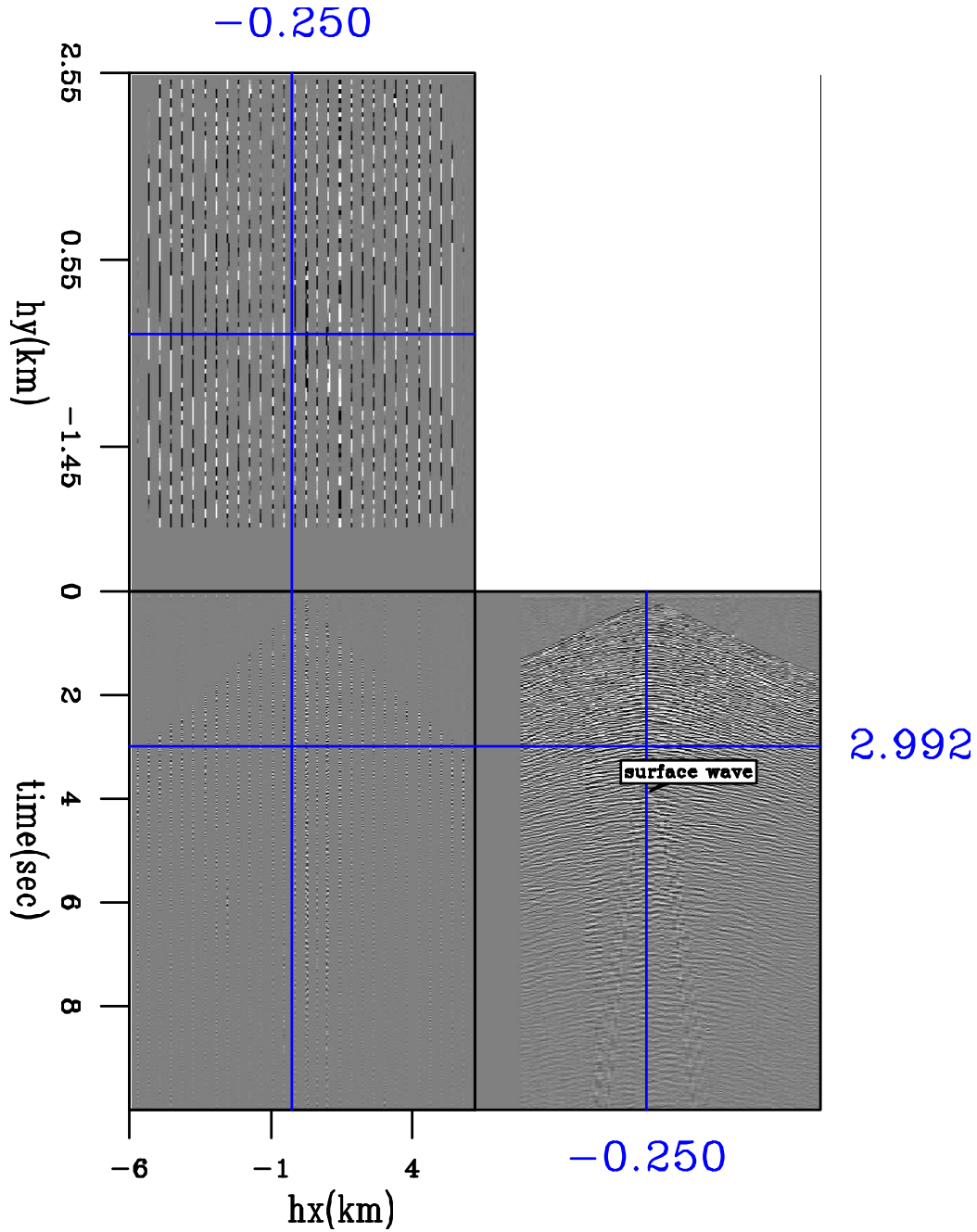


Figure 4.9: One receiver gather shows the dense cross-line sampling and very coarse in-line sampling. The slow arrivals after 3.5 s are the low frequency surface wave energies. [ER] `chap4/.recgth1`

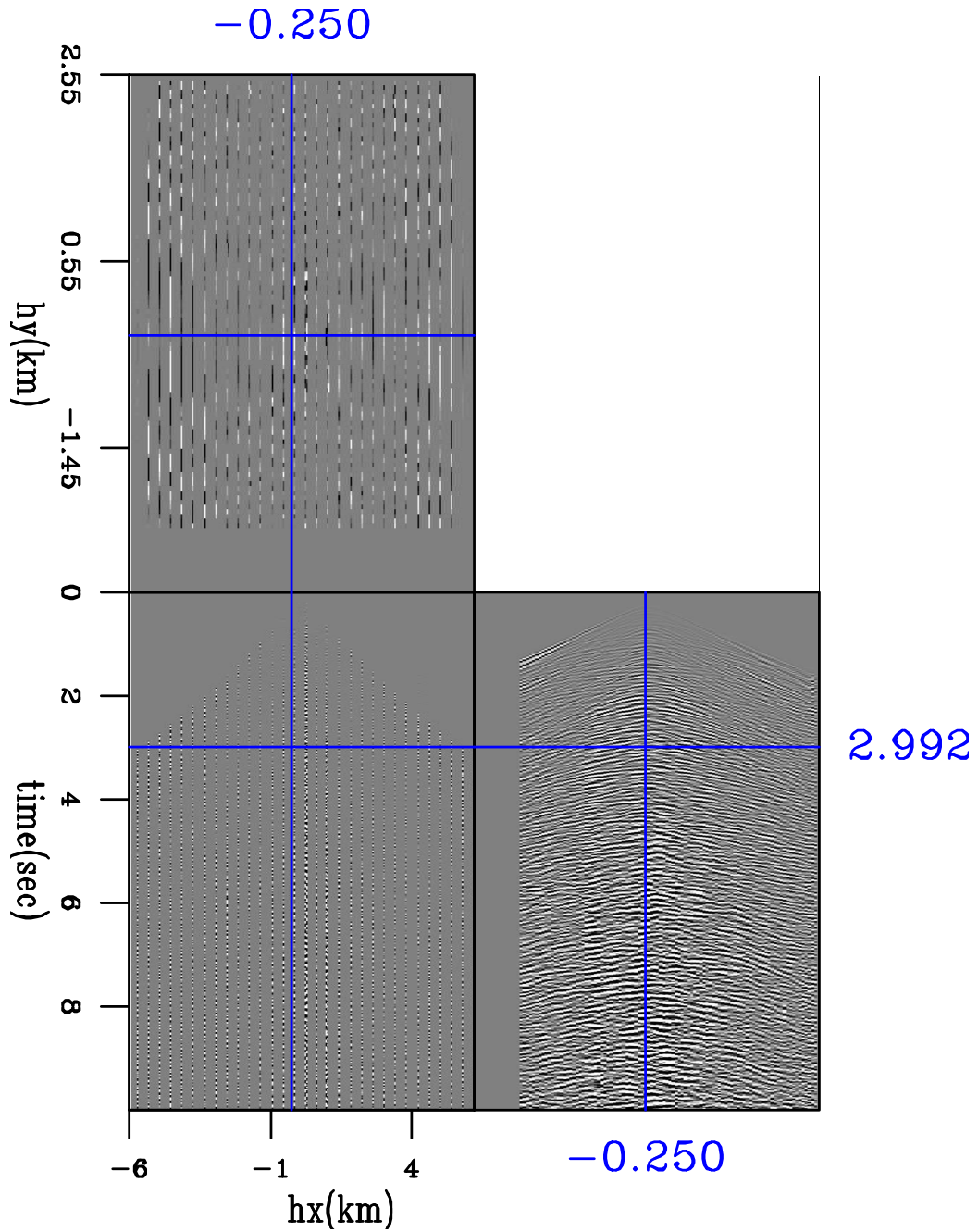


Figure 4.10: Receiver gather in Figure 4.9 after bandpass, muting and time weighting. Surface waves have been attenuated. Reflection events become more continuous especially in the later time. [ER] `chap4/. recgth1-proc`

The salt body and the water column are considered isotropic. It is reasonable to assume that the tomographic isotropic velocity (Figure 4.11(a)) best estimates the NMO velocity in a VTI parameterization. Therefore, I compute the anisotropic vertical velocity model 4.11(b) from the δ model (Figure 4.11(d)) and the isotropic NMO velocity (Figure 4.11(a)). The vertical velocity is slightly smaller than the NMO velocity due to a positive δ model.

Figure 4.12 and Figure 4.13 compare the images between the isotropic migration and the anisotropic migration at two different locations. Compared with Figure 4.12(a), the depths of the flat reflectors in the anisotropic migration image (Figure 4.12(b)) remain roughly the same due to a small δ value. Nevertheless, the focusing of these shallow flat events are improved by the anisotropic model. The depth slice of the anisotropic migration image shows better coherence and higher resolution on the discontinuities across the fault (labeled 1). The dipping reflectors in the in-line direction (highlighted by oval) and the strong near-horizontal reflector above 6 km (labeled 2) in the cross-line direction are also more continuous in the anisotropic migration image. Comparison between Figure 4.13(a) and Figure 4.13(b) shows similar qualities in both migration images. The crossing events and broken reflectors below 4 km in the cross-line direction indicate better models are needed to properly focus the image. These images demonstrate a typical case where two different models, with completely different geological implications, can explain the seismic traveltimes equally well.

To update the anisotropic model, I use the anisotropic WEMVA scheme (Chapter 3). However, the computational and memory requirement to build the subsurface offset common image gathers (SOCIGs) and hence the angle domain common image gathers (ADCIGs) are prohibitively expensive. Furthermore, the migration image based on the initial VTI model is relatively well focused. Therefore, I assume the initial model is close enough to the true solution, and drop the differential semblance term in the objective function.

The anisotropic WEMVA objective function I minimize in this chapter reads as

follows:

$$S(\mathbf{m}) = -\frac{1}{2} \left\| \sum_{\theta} \mathbf{I}(\mathbf{x}, \theta) \right\|^2 + \frac{\alpha}{2} (\mathbf{m} - \mathbf{m}_{\text{prior}})^T \mathbf{C}_M^{-1} (\mathbf{m} - \mathbf{m}_{\text{prior}}), \quad (4.1)$$

where the first term defines the “data fitting” objective by maximizing the stacking power, and the second term defines the “model regularization” objective by including the geological and the rock physics information through the initial model $\mathbf{m}_{\text{prior}}$ and the covariance matrix \mathbf{C}_M . Parameter α balances the relative weights between the two objectives. During implementation, the stack image $\sum_{\theta} \mathbf{I}(\mathbf{x}, \theta)$ is simply computed using the cross-correlation imaging condition at zero subsurface offset in both in-line and cross-line directions.

Each anisotropic WEMVA iteration has three main computation-intensive steps: migration, gradient computation, and the line search process. I summarize the computational cost during each anisotropic WEMVA iteration in Table 4.1. Computation time for each process is measured on a single node with OpenMP parallelization over 16 processors. Assuming 60 nodes are always available, it takes 56 hours to finish one WEMVA iteration.

Table 4.1 shows that the most expensive processing step is the gradient computation. To reduce the computation cost, I take advantage of the redundancy in shots during the gradient computation. During each iteration, I randomly select one-third of the shots to perform the tomographic gradient calculations. The inaccuracy introduced by the subsampling is insignificant for two reasons: first, the subsampling artifacts are dominated by higher wavenumber components, especially in the horizontal direction. These artifacts are mitigated by the structural smoothing process; second, artifacts introduced in the current iteration are incoherent with the inaccuracies in the next iterations when another set of random shots are used. Therefore, the stacking of the updates over iterations will also suppress the artifacts in the gradients.

The subsampling strategy is not applied for the migration and the line search steps although it would greatly reduce the computational cost. The reasons for not applying the subsampling strategy are two fold. First, dense sampling in shots are needed to

fully collapse the migration smiles due to the sparse cross-spread acquisition geometry. Second, the stacking power objective function is very sensitive to the artifacts in the migration image, which could be translated into unrealistic model updates.

To demonstrate the redundancy of the shots when computing the gradients, I show the gradient in vertical velocity using all the shots in Figure 4.14(a). The gradient has been smoothed along the structure dips estimated from the initial migration image. A fast velocity anomaly centered at $x = 9$ km and $y = 15$ km dominates the gradient.

The gradient using only a third of the shots is shown in Figure 4.15(a). Due to the reduced number of stacked shots, the amplitudes of the gradients are reduced. Nonetheless, the structures of the updates are remarkably similar except for minimal amplitude shifts. Therefore, I can safely reduce the number of shots in gradient computation without introducing significant errors. Similar comparison and conclusions can be made for the gradients of ϵ and δ (compare Figures 4.14(b) with 4.15(b), and Figures 4.14(c) with 4.15(c)).

I summarize the non-linear conjugate gradient optimization workflow in Algorithm 3. With the random shot reduction (shown between parenthesis in Table 4.1), the total time for one WEMVA iteration is reduced to 36 hours.

Process	Time/Shot (min)	# of Shots
Migration	7	3500
Gradient computation	30	3500 (1167)
Line search	21	3500

Table 4.1: Computational cost for each WEMVA iteration.

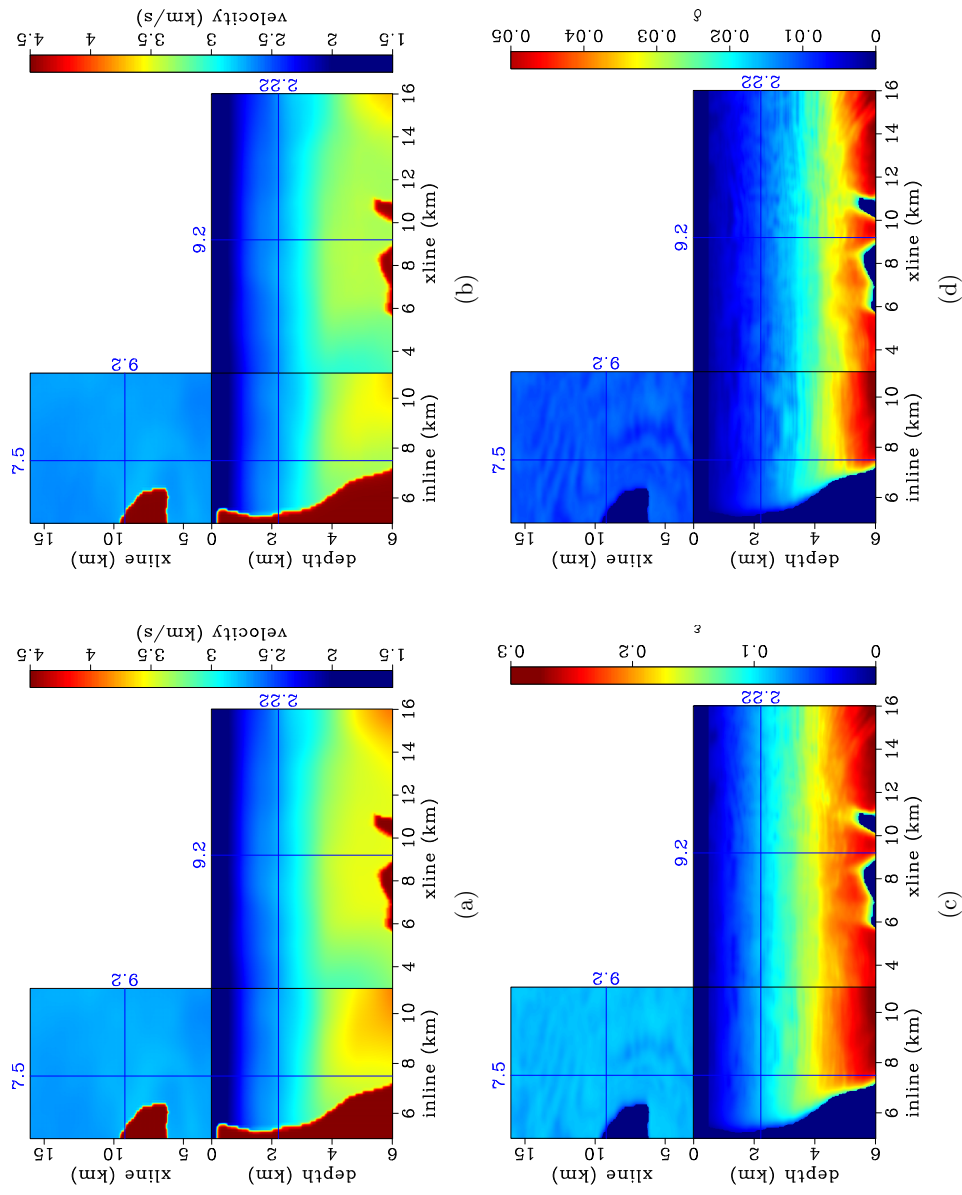


Figure 4.11: (a): Isotropic velocity model provided by ray-based tomography. (b): Vertical velocity tomography. (c): initial ϵ model and (d): initial δ model from the rock physics modeling. [CR]

chap4/ iso-vel,v0-iter0,eps-iter0,delta-iter0

Algorithm 3 Optimization algorithm

initialize the model: \mathbf{m}_0
 compute the migrated image: I_0
 randomly select 1/3 of all shots
 compute the gradient: \mathbf{g}_0
 precondition the gradient: $\mathbf{g}_s^0 = \mathbf{S}\Sigma\Sigma^*\mathbf{S}^*\mathbf{g}_0$
 initialize the search direction: $\mathbf{p}_0 = -\mathbf{g}_s^0$
for $k = 1 \dots N_k$ **do**
 perform a line search: optimize λ , $\operatorname{argmin}_\lambda J(\mathbf{m}_{k-1} + \lambda\mathbf{p}_{k-1})$
 update the velocity model: $\mathbf{m}_k = \mathbf{m}_{k-1} + \lambda\mathbf{p}_{k-1}$
 compute the migrated image: I_k
 randomly select 1/3 of all shots
 compute the gradient: \mathbf{g}_k
 precondition the gradient: $\mathbf{g}_s^k = \mathbf{S}\Sigma\Sigma^*\mathbf{S}^*\mathbf{g}_k$
 find the search direction: $\mathbf{p}_k = -\mathbf{g}_k + \frac{(\mathbf{g}_s^k)^T(\mathbf{g}_s^k - \mathbf{g}_s^{k-1})}{(\mathbf{g}_s^{k-1})^T\mathbf{g}_s^{k-1}}$
end for

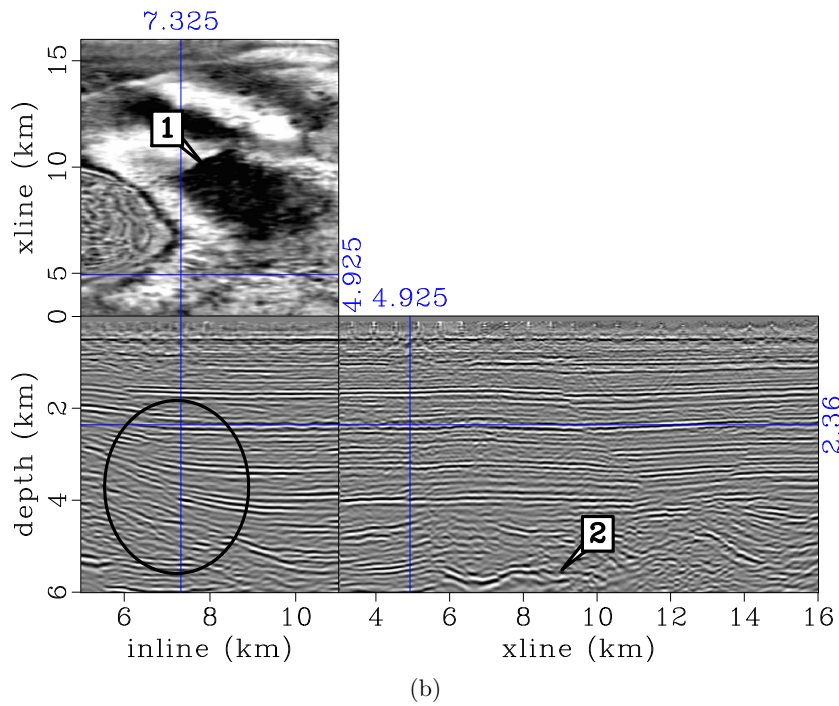
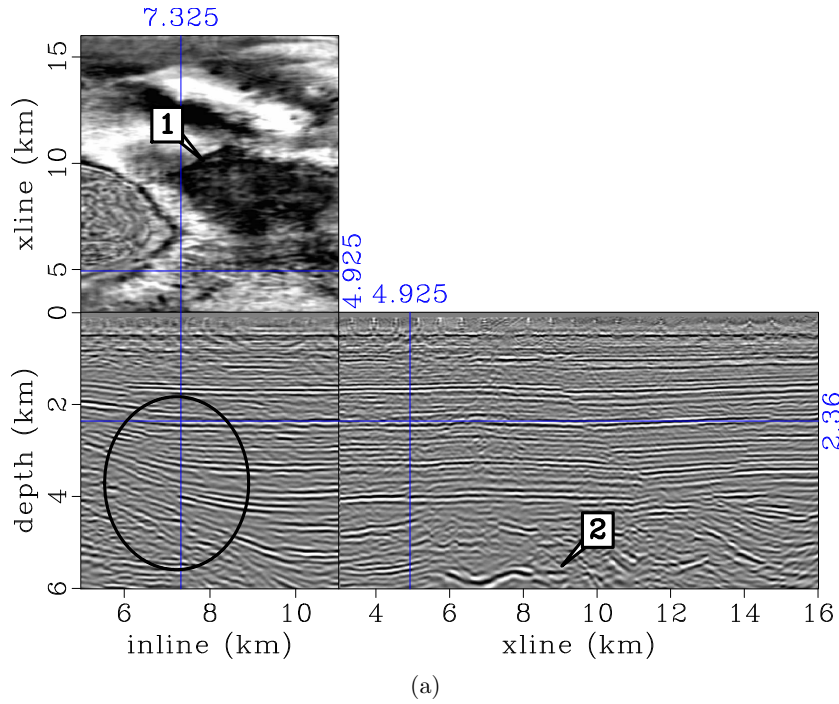


Figure 4.12: (a): Isotropic migration image using the isotropic velocity in Figure 4.11(a). (b): Anisotropic migration image using the models in Figure 4.11(b) to 4.11(d). [CR] chap4/. iso-img2,ani-img2

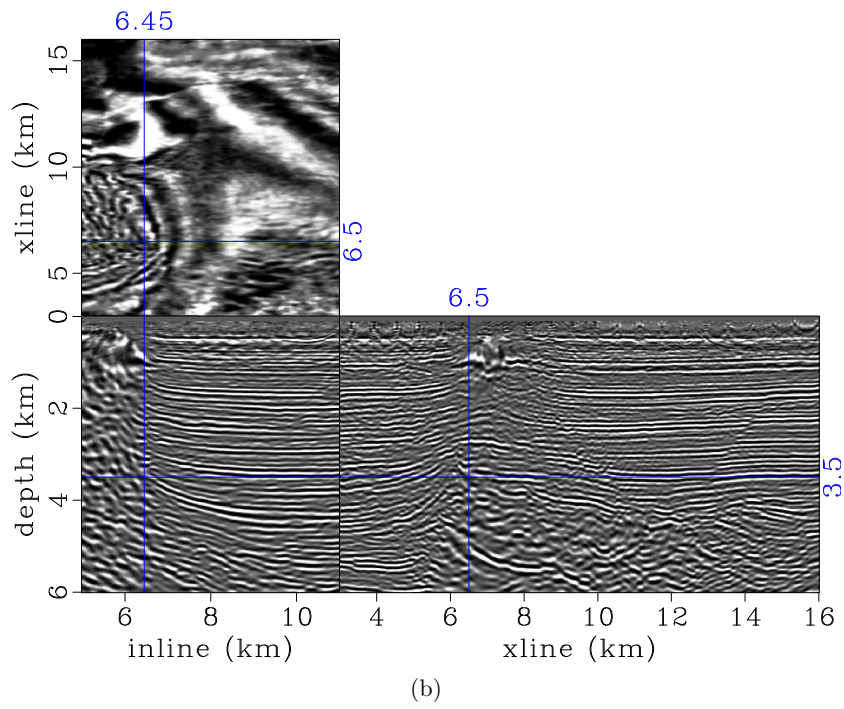
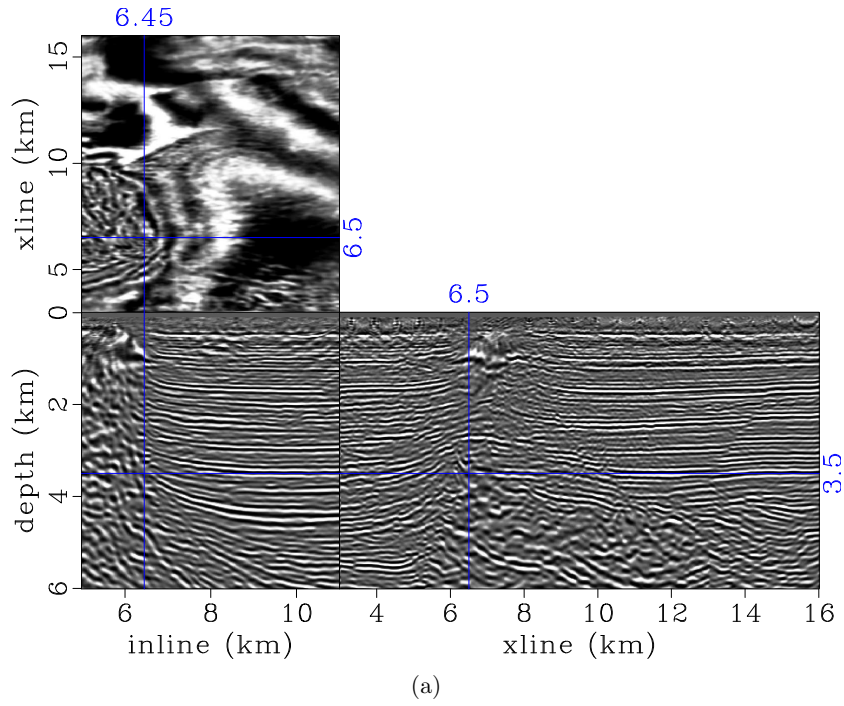


Figure 4.13: Same as Figure 4.12 but at a different location. [CR]

chap4/. iso-img1,ani-img1

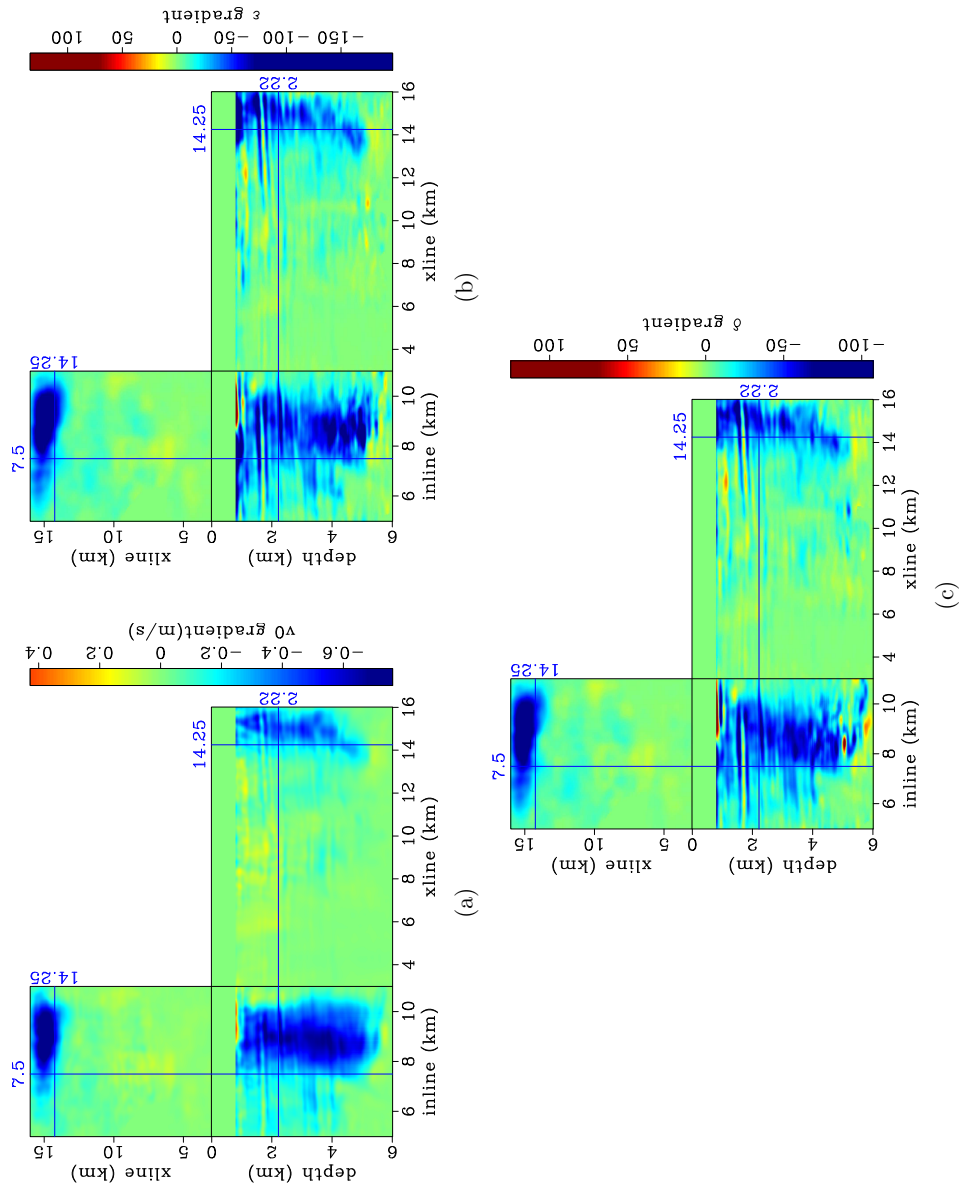


Figure 4.14: First anisotropic WEMVA gradient of (a) vertical velocity, (b) ϵ , and (c) δ using all shots. [CR]
 chap4/. gvel-all-raw,geps-all-raw,gdel-all-raw

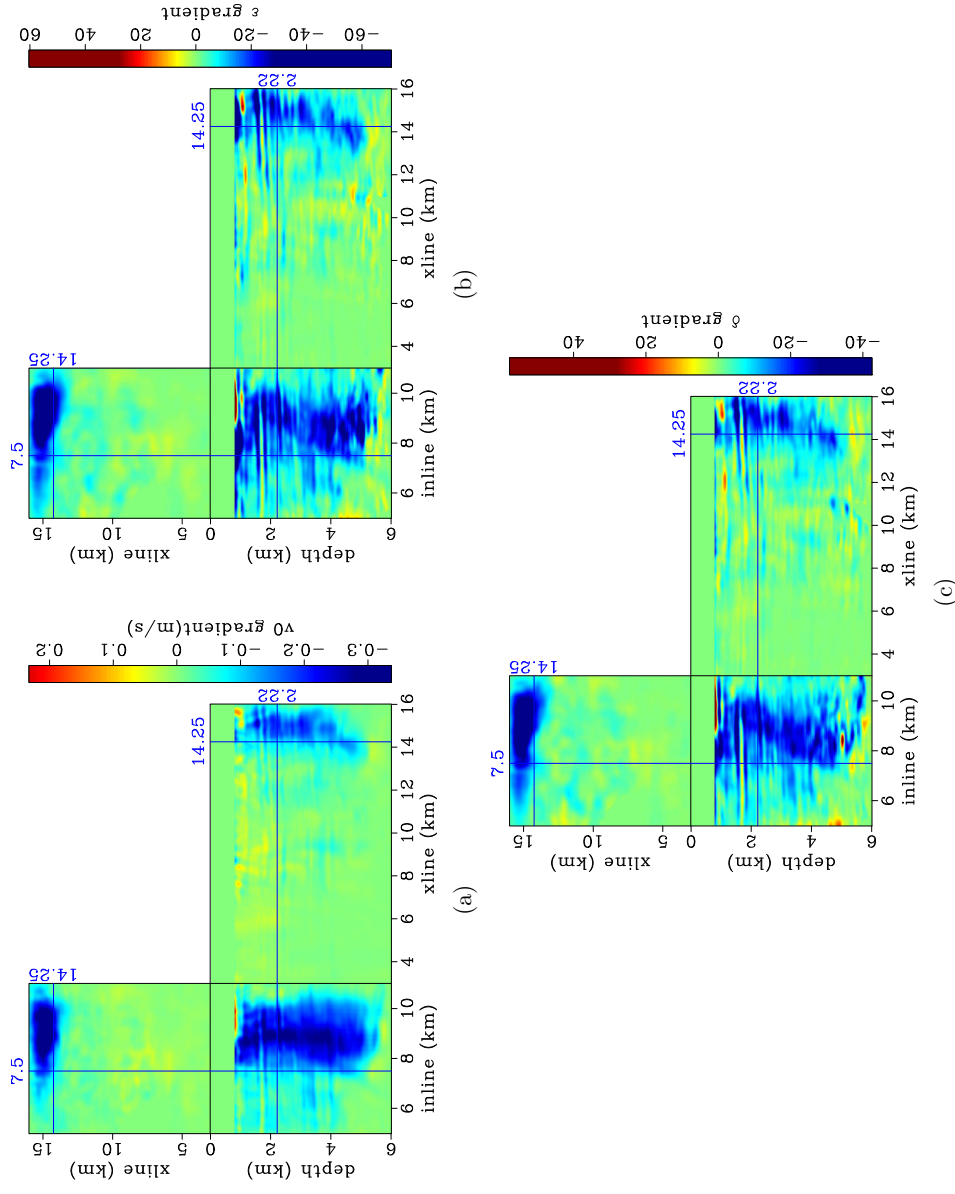


Figure 4.15: First anisotropic WEMVA gradient of (a) vertical velocity, (b) ϵ , and (c) δ using one-third of all the shots. [CR] chap4/. gvel-third-row,geps-third-row,gdel-third-row

Compared with the gradient in vertical velocity (Figure 4.15(a)), the gradients in ϵ (Figure 4.15(b)) and δ (Figure 4.15(c)) show similar structures and point to the same update directions. These updates are determined by the WEMVA tomographic operator so that they increase the stacking power constructively. However, it is unrealistic for a shallow layer to have both positive velocity and positive anisotropy based on the lithological inversion results and our rock physics prior knowledge.

To honor the rock physics prior information, we apply the cross-parameter covariance matrix (Figures 4.4 and 4.5) in the preconditioning. As a result, the gradient direction in ϵ (Figure 4.16(b)) and δ (Figure 4.16(c)) in the shallow region has been reversed based on the negative correlation between velocity and anisotropy. These preconditioned gradients (Figure 4.16) are used in a Polak-Ribière nonlinear conjugate gradient scheme (Wright and Nocedal, 1999) to calculate the update direction.

I use a three-point parabolic interpolation scheme (Box et al., 1969) to conduct a line search. The line search algorithm evaluates the objective function with three different step lengths. Then a parabola is fitted to find the minimum and its corresponding step length. This line search scheme is exact when the objective function is parabolic near its bottom. However, the shape of the objective function is not guaranteed parabolic in the case of nonlinear inversion. Therefore, I compare the four trial step lengths with the objective function in the previous iteration, keep the lowest objective function, and update the model with the corresponding step length.

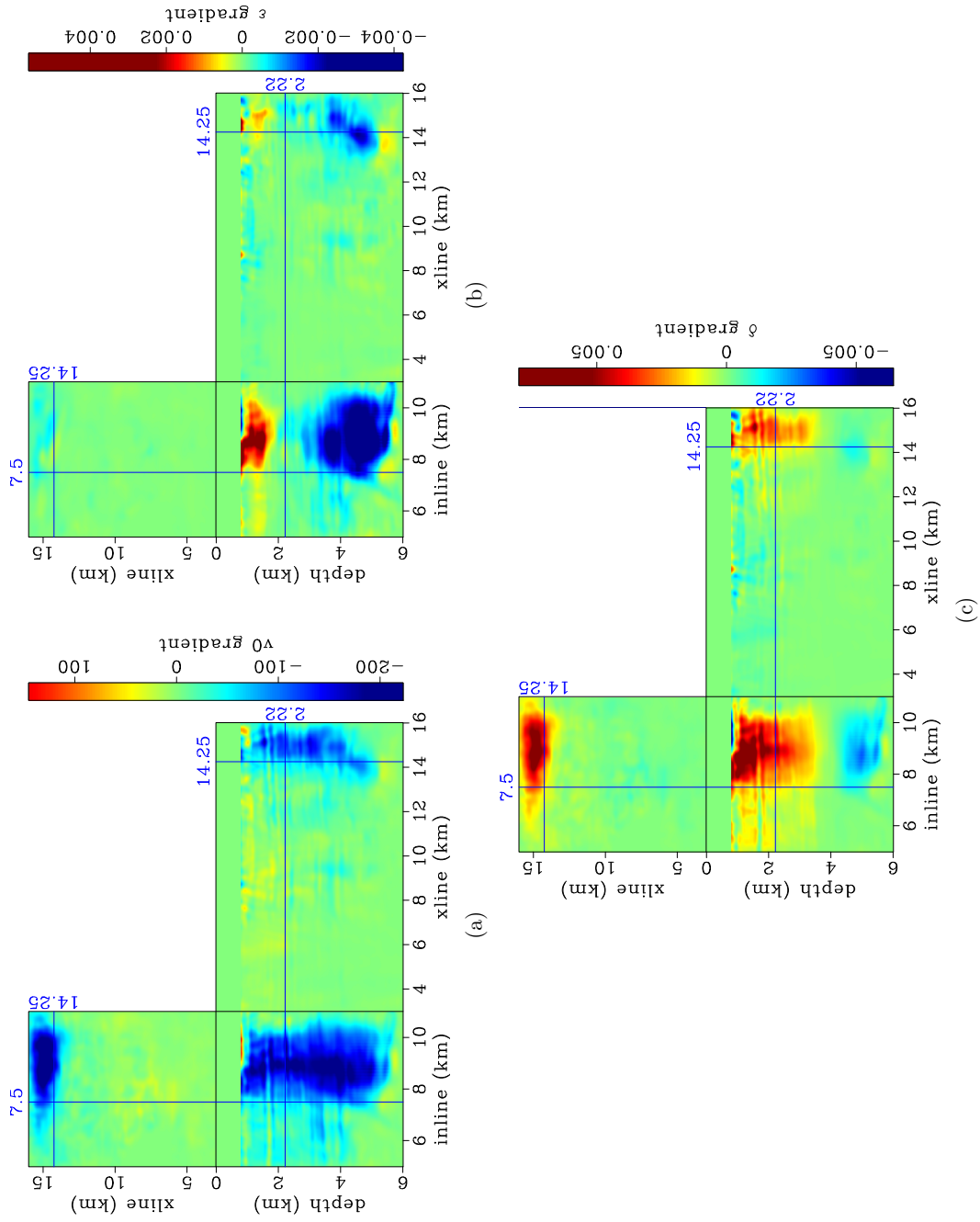


Figure 4.16: First anisotropic WEMVA gradient of (a) vertical velocity, (b) ϵ , and (c) δ after rock physics preconditioning. [CR] chap4/. gvel-third-prc.geps-third-prc.gdel-third-prc

Inversion results

In this subsection, I present the inversion results after ten nonlinear anisotropic WEMVA iterations. Both the normalized stacking power curve (Figure 4.17(a)) and the normalized gradient magnitude curve (Figure 4.17(b)) demonstrate a fast convergence in the first few iterations. The stacking power curve flattens out after seven iterations. Although the inversion still updates the VTI model in the last three iterations, these updates do not affect the focusing of the seismic image.

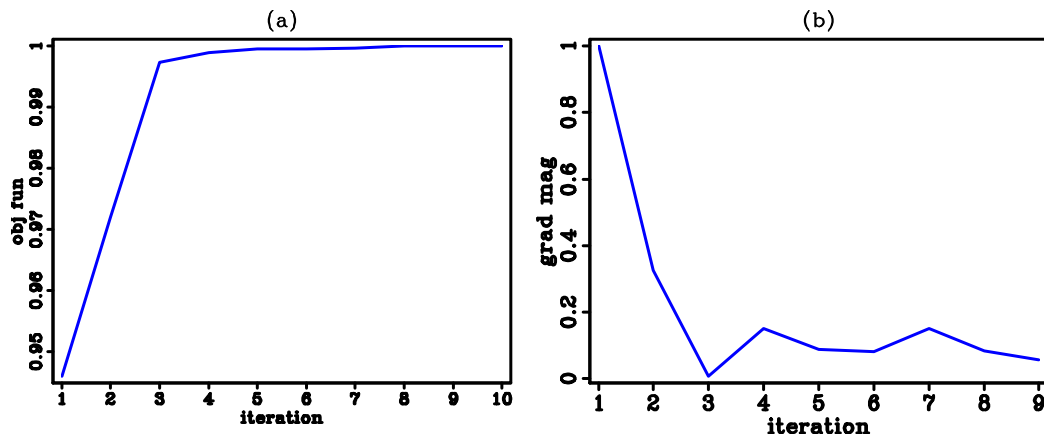


Figure 4.17: (a): Normalized stacking power curve. (b): Normalized gradient magnitude curve. Both curves show fast convergence in the first few iterations. [CR] chap4/. dragon-converge

Figure 4.18 shows the total updates in the VTI model after ten nonlinear iterations. The inversion identifies a positive velocity anomaly on the footwall of the normal fault, which can be caused by the regional stress distribution. To consistently produce a high velocity rock in the shallow region, the regularization scheme reduces the anisotropy in the corresponding region, indicating a stronger sand-dominated sedimentary environment. In the deeper region, both velocity and anisotropy are positively updated due to the strong diagenesis in the shale. Significant updates are also shown around the salt body where the initial ray-based tomography failed to update.

It is interesting to note that the negative correlation between velocity and δ extends deeper than the negative correlation between velocity and ϵ . However impossible to be obtained from the seismic data inversion, it is consistent with the rock physics prior information. On average there are 5% positive updates in vertical velocity and more than 10% updates in both ϵ and δ .

Figure 4.19 shows the updated VTI model. All three VTI parameters are smooth along the structure dip direction, which agrees with our geological assumptions. All three VTI parameters are consistent with the rock physics model I choose to apply, because I constrain both the initial model and the model updates during each iteration.

Figures 4.20 and 4.21 compare the migration images with the initial model with the migration image with the updated model at a cross-line location near the salt flank. Reflectors in both in-line and cross-line directions are strongly dipping. Highlighted by circles labeled 2 and 3, these reflectors are broken in the initial migration image, making the interpretation of the sediments around the salt body a challenging task. The updated model revealed a much clearer image around the salt. Reflectors in both areas are better imaged with more continuity and better resolution. The improved resolution is also shown on the depth slice. Flag 1 points out a fault which is blurred in the initial migration image but distinctly imaged with the updated model.

Similar improvements can be observed on the other side of the salt flank. The sediment reflectors are ambiguous from the initial migration image (Figure 4.22), as highlighted by the labeled circles. The truncation effects of the sedimentary layers against the salt body are better imaged with the improved model (Figure 4.23), providing higher confidence for salt body interpretation. Moreover, a set of faults caused by the salt intrusion (label 1) is much better focused on the depth slice with the improved anisotropic model.

Figure 4.24 and 4.25 cut through the image cube near the strongest model updates. On the in-line section, the strong reflectors are imaged deeper and more continuous with a higher velocity (circle 2). On the cross-line section, two normal faults (one is

highlighted by circle 3) are much more distinct due to the improved focusing. On the depth slice, the resolution of the sediments around the salt body are much higher in the updated image.

In Figures 4.26 to 4.28, I compare the angle-domain common image gathers before and after update. The initial ADCIGs are reasonably flat, only with minor residual moveouts. Nevertheless, the flatness of the ADCIGs has been improved with the updated VTI model. Without changing depth, the ADCIGs show increased angle coverage in the shallow region, mostly due to the improved definition of the Thomsen parameters ϵ and δ . Overall, the increased flatness and angle coverage produces a better focused image. These angle events can certainly help the interpretation and the AVA analysis.

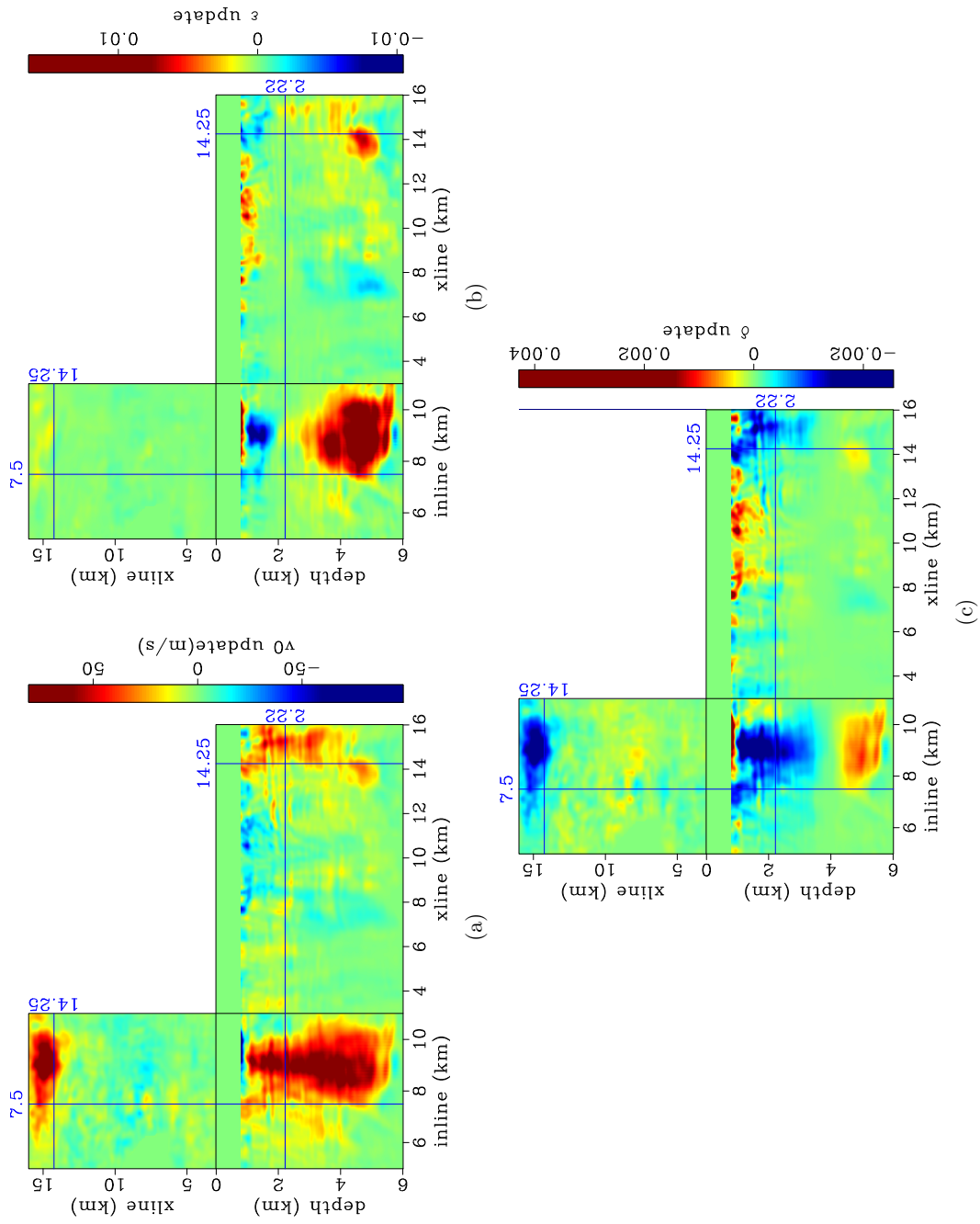


Figure 4.18: Total updates after ten anisotropic WEMVA iterations in (a): vertical velocity model, (b): ϵ model and (c): δ model after ten anisotropic WEMVA iterations. [CR] chap4/. vel-updt-all,eps-updt-all,delta-updt-all

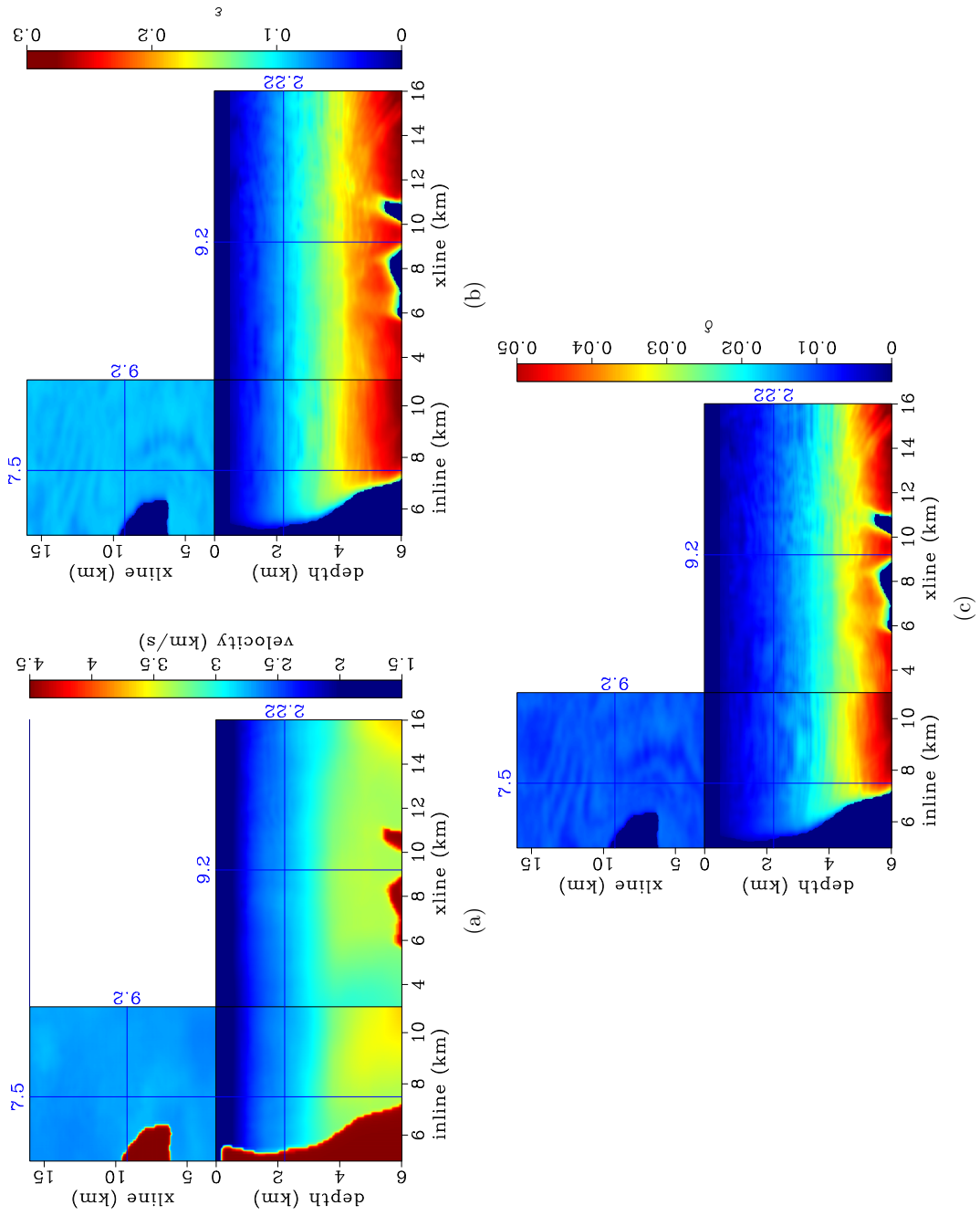


Figure 4.19: (a): Vertical velocity model, (b): ϵ model and (c): δ model after ten anisotropic WEMVA iterations.

[CR] chap4/. v0-final,eps-final,del-final

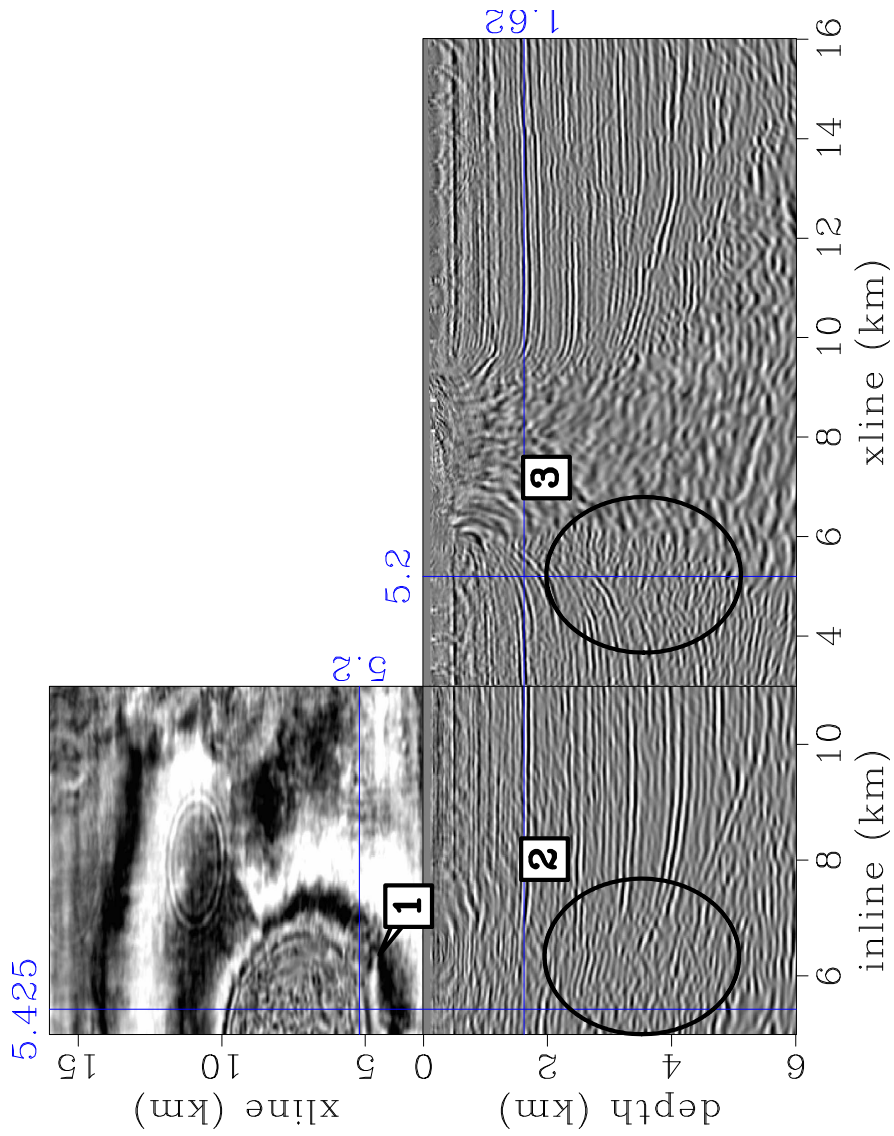


Figure 4.20: Migration image using the initial anisotropic model. Labels 2 and 3 highlights areas with broken reflectors in the in-line and cross-line direction, respectively. [CR] chap4/. ani-iter0-1

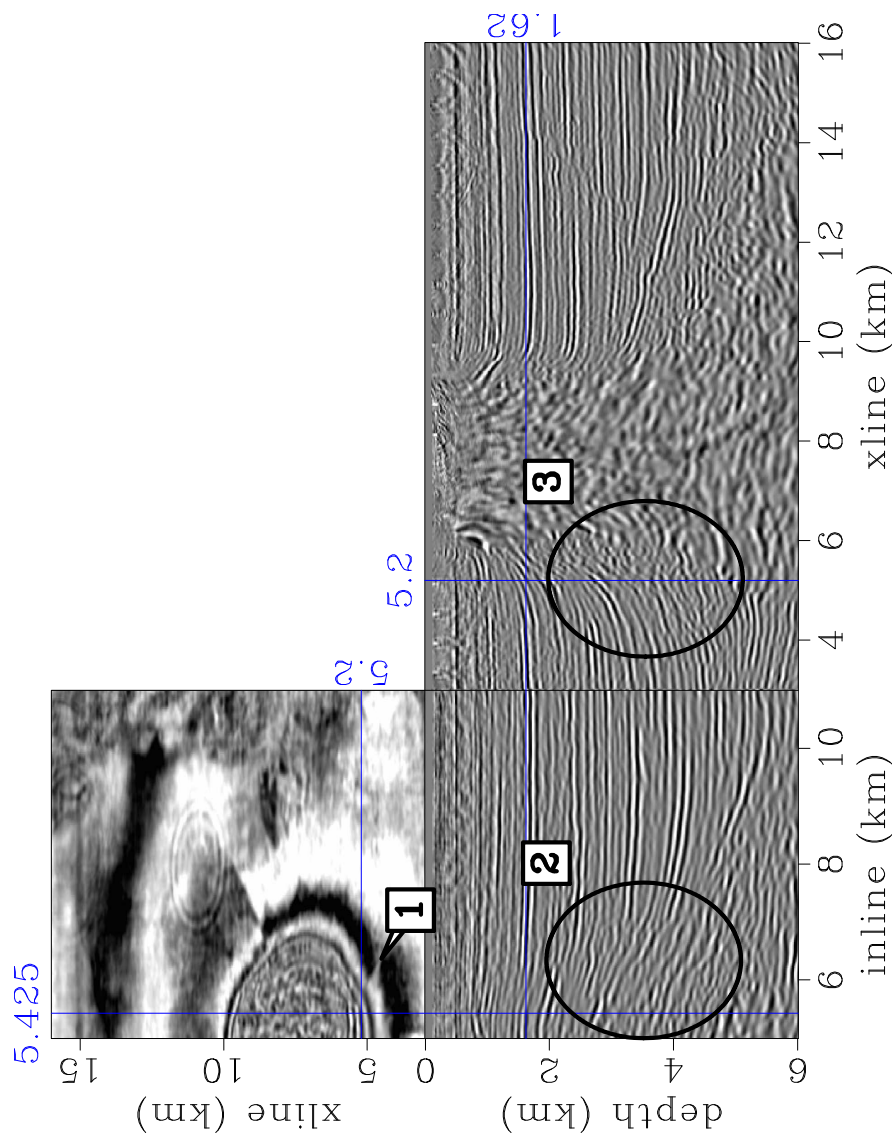


Figure 4.21: Migration image using the updated anisotropic model after ten iterations. Comparing to Figure 4.20, label 1 points out a distinct fault near the salt body which is much better imaged with the updated model. Dipping Reflectors in both circles 2 and 3 are more continuous. [CR] chap4/. ani-iter10-1

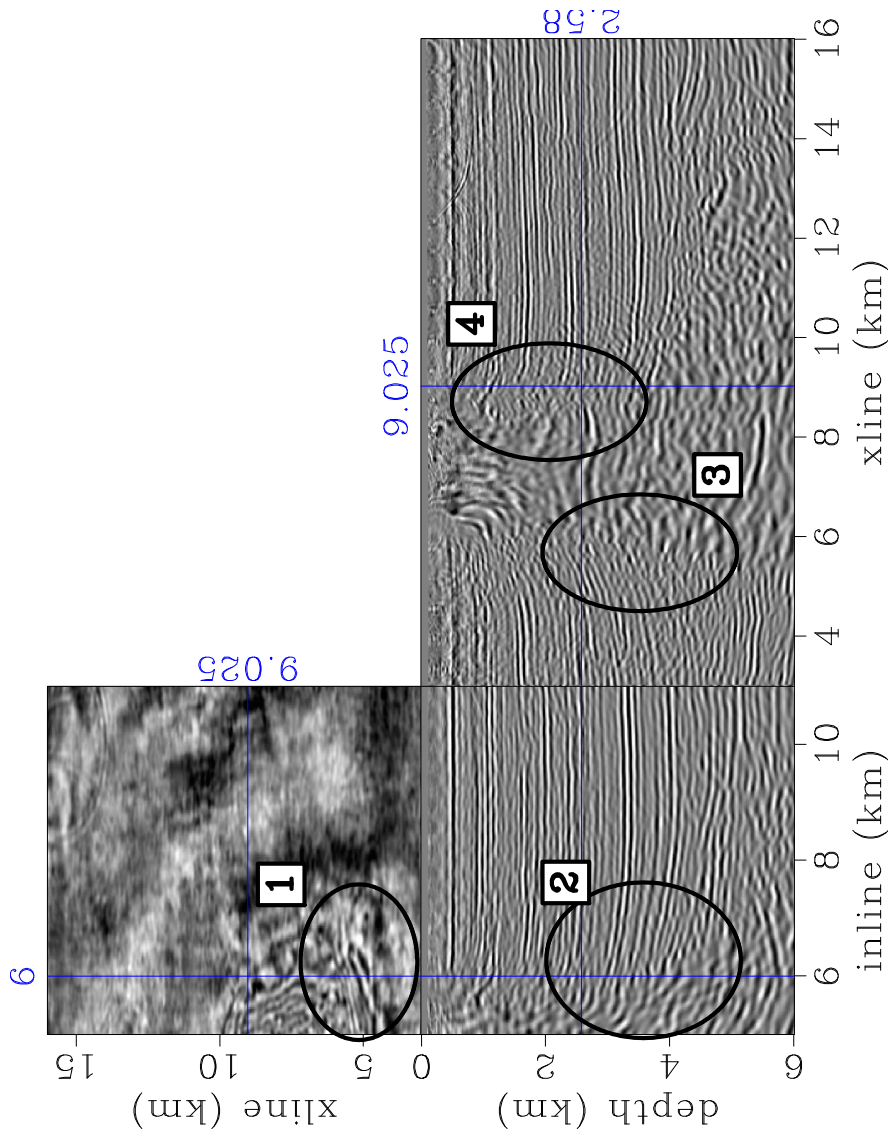


Figure 4.22: Migration image using the initial anisotropic model. Sediments truncation and salt flank are ambiguous in circle 2, 3, and 4. [CR] chap4/. ani-iter0-2

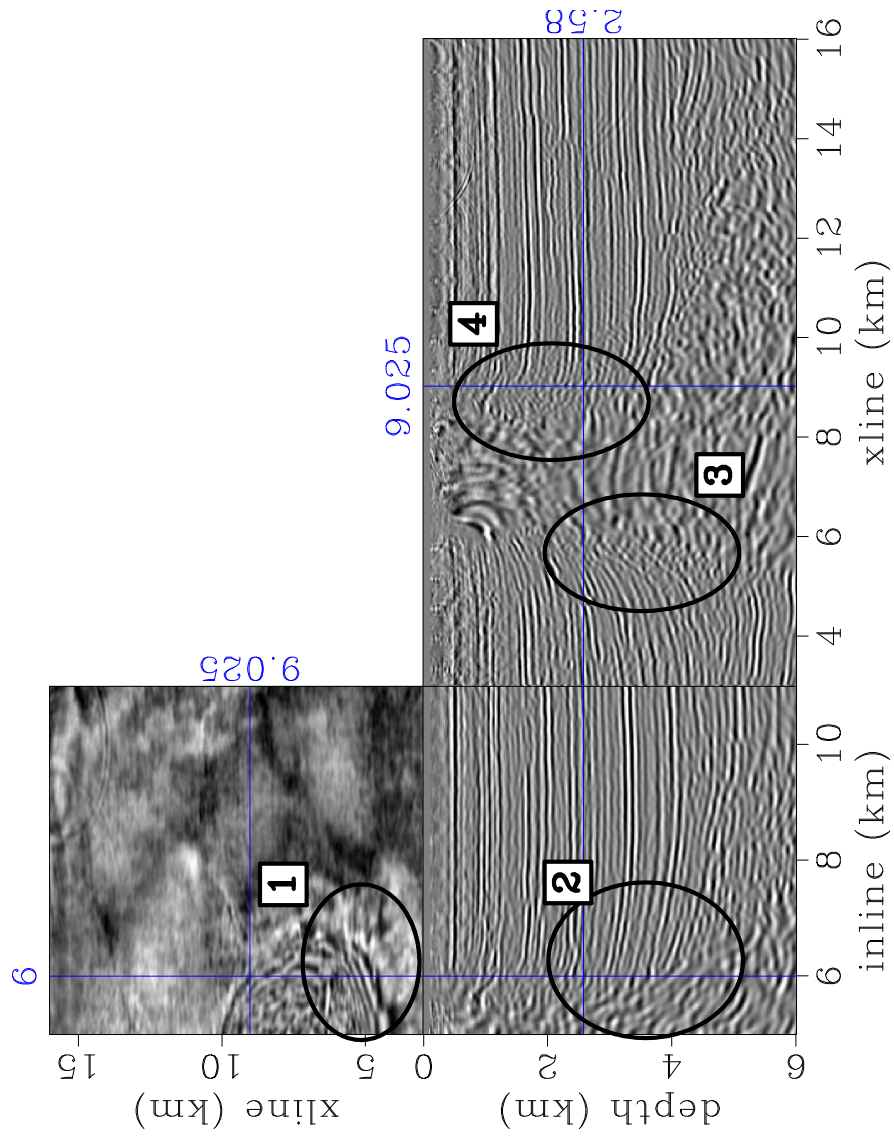


Figure 4.23: Migration image using the updated anisotropic model. Compared to Figure 4.22, sediments truncation and salt flank are much better imaged. On the depth slice, a set of faults (circle 1) caused by the salt intrusion are better focused. [CR] chap4/. ani-iter10-2

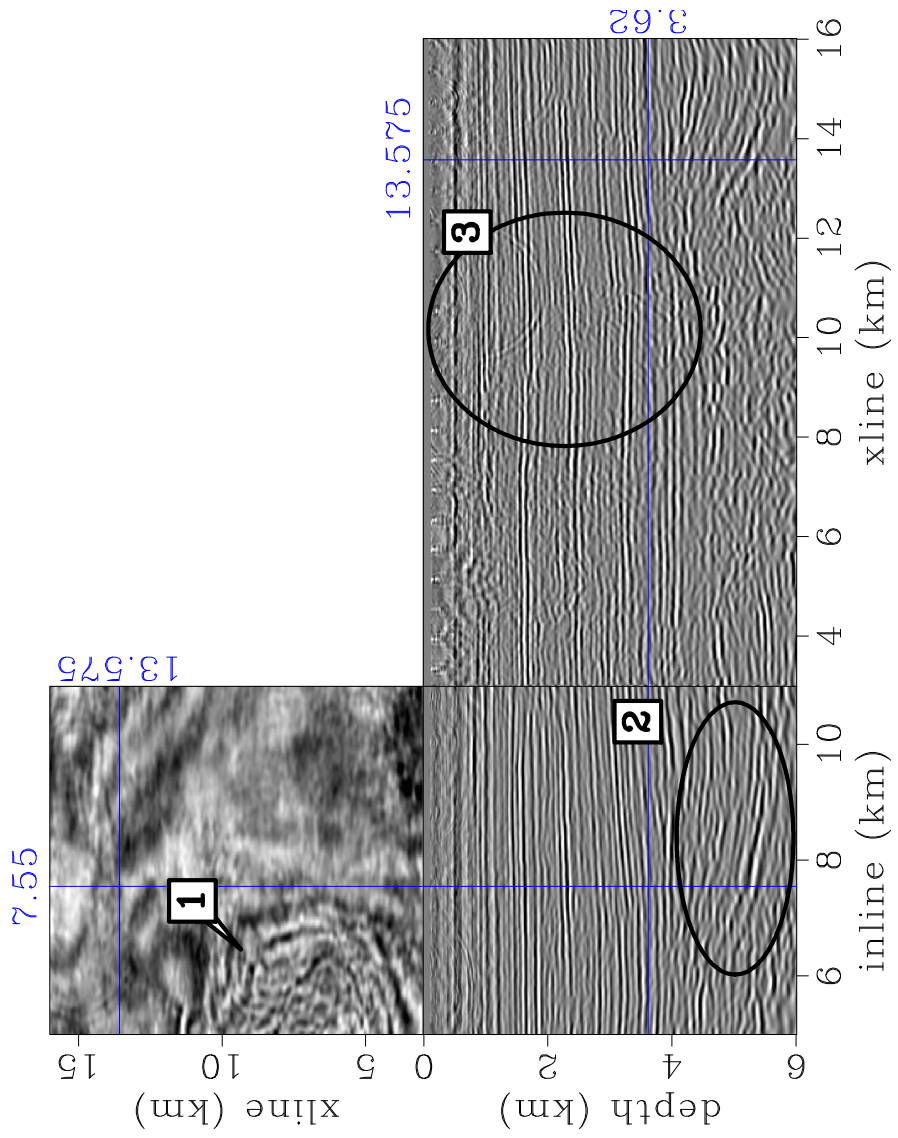


Figure 4.24: Migration image using the initial anisotropic model. [CR] chap4/. ani-iter0-3

DISCUSSION

Earth model building is a highly underdetermined problem and uncertainties propagate from each step of the model building process. In this study, I include the uncertainties of the rock physics modeling by sampling the distribution of the input parameters and by using two different effective medium models. However, there are certainly more uncertainties with different geological scenarios which have been neglected. Moreover, the seismic data inversion is also nonunique. The current inversion practice of producing a single solution lacks uncertainty analysis, which can be highly valuable for decision making and risk management.

Using previous seismic inversion results to constrain the seismic model building in the next iteration helps us close the loop linking seismic data with reservoir modeling. Traditional processing from seismic data to a reservoir model does not include feedback; and the seismic data modeled from the inverted reservoir model usually do not match the field data. This study provides a step toward building a closed loop from exploration to production. With more iterations, Earth models that are consistent with all the available data could be obtained and their uncertainties should be evaluated.

CONCLUSIONS

In this chapter, I tested the rock physics constrained anisotropic WEMVA method on a 3-D field data set. I first build the rock physics constraints using stochastic rock physics modeling and then utilize these constraints during the anisotropic WEMVA inversion to produce reliable VTI models as well as better focused images.

Stochastic rock physics modeling is a powerful tool to model the shale anisotropy and to explore the possible ranges of the anisotropic parameters. By sampling the distributions of the key parameters, I include their uncertainties and produce an ensemble of anisotropic models which are realizable by rock physics modeling. The field data example demonstrates that it is reasonable to assume a multivariate Gaussian

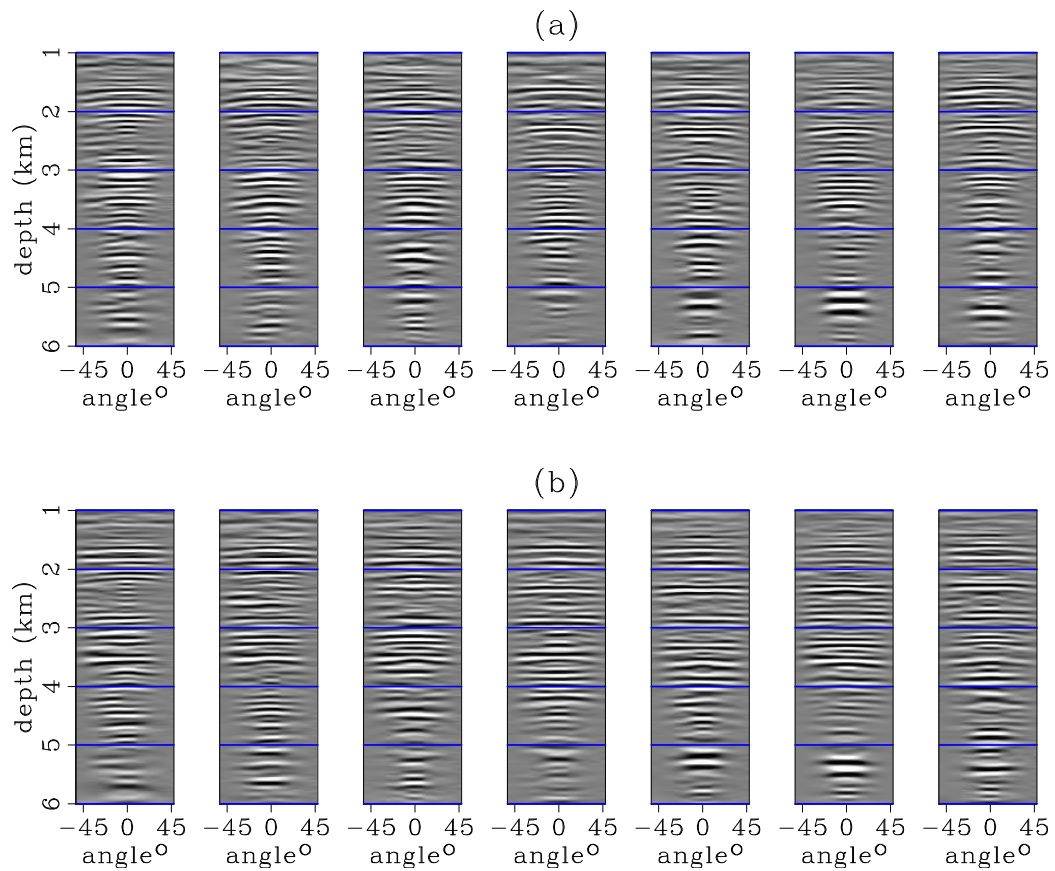


Figure 4.26: ADCIGs using the initial model (a) and the updated model (b). ADCIGs are extracted from $y = 13.5$ km and $x = 6, 6.5, 7, 7.5, 8, 8.5, 9$ km from left to right. The downward curvatures in the shallow gathers (above 2 km) are flattened in the updated ADCIGs. Angle coverages of the ADCIGs at medium depths (between 2 km and 4 km) are improved, especially for the horizon at roughly 3.5 km depth. In the deep section, the updated ADCIGs show wider angle coverage and higher resolution.

[CR] chap4/. adcig-x-y13500

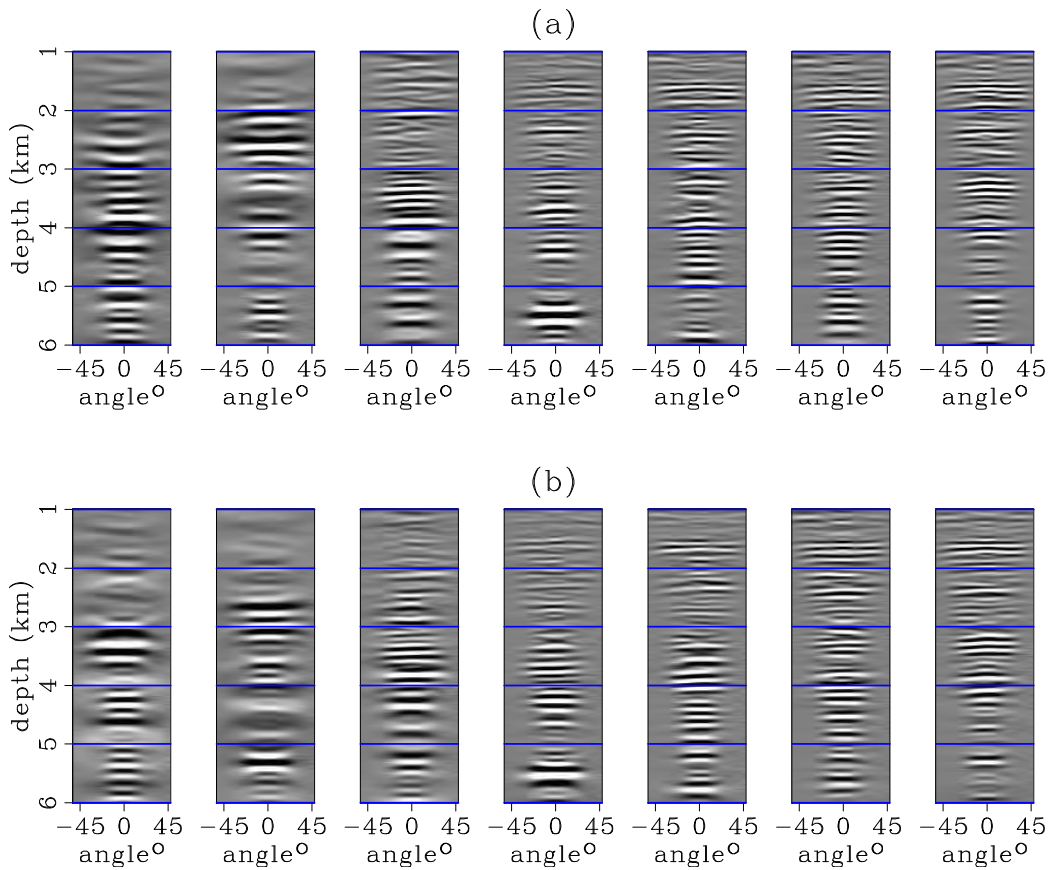


Figure 4.27: ADCIGs using the initial model (a) and the updated model (b). ADCIGs are extracted from $y = 7.5$ km and $x = 6, 6.5, 7, 7.5, 8, 8.5, 9$ km from left to right. ADCIGs are extracted close to the salt body. Due to the improved VTI model, updated ADCIGs show flatter events with stronger energy. [CR] `chap4/.adcig-y-y7500`

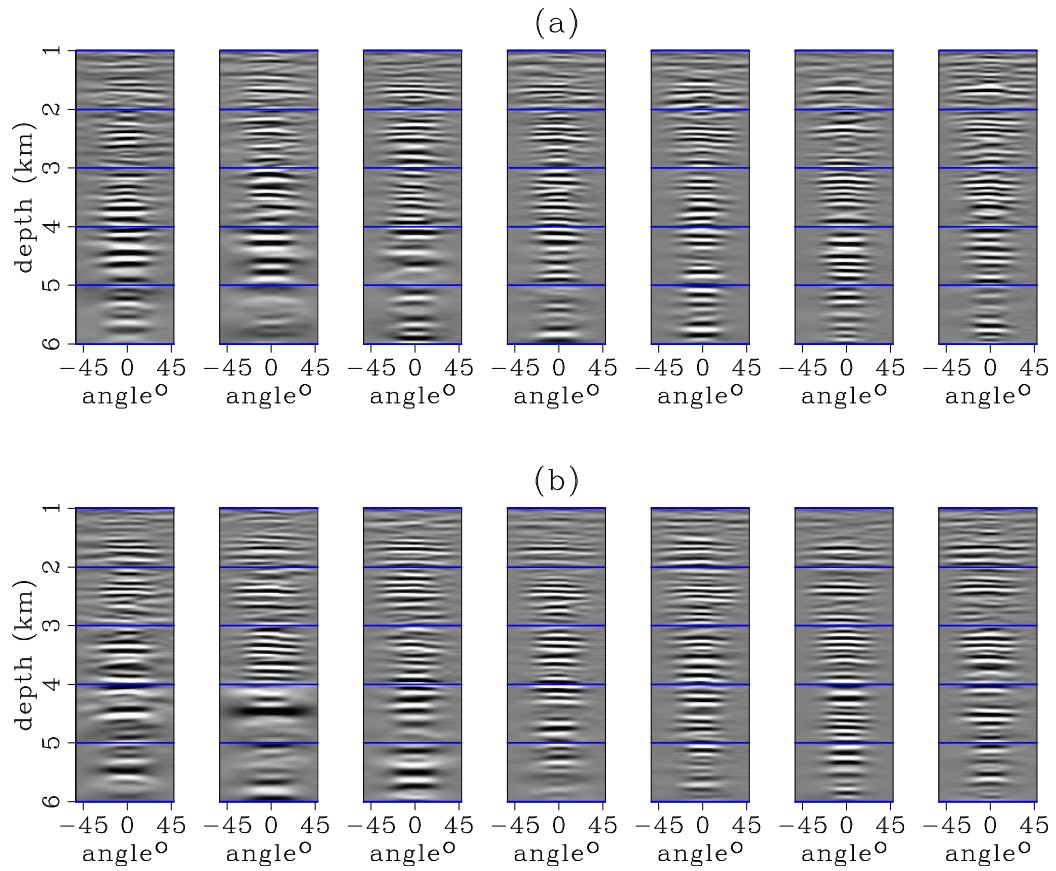


Figure 4.28: ADCIGs using the initial model (a) and the updated model (b). ADCIGs are extracted from $y = 10$ km and $x = 6, 6.5, 7, 7.5, 8, 8.5, 9$ km from left to right. Updated ADCIGs show strong improvements below 4 km (more significantly on the three left panels) due to the cumulative effects of anisotropy along the wavepaths.

[CR] chap4/. adcig-y-y10000

distribution and summarize the random variables using the mean and the covariance matrix. Migration images based on the mean model demonstrate that the rock physics modeling produces good initial anisotropic models for seismic imaging. A 3-D prior distribution model is made possible by utilizing the lithological inversion results of a previous seismic processing workflow.

By constraining the anisotropic WEMVA with the geological and rock physics covariance, I feed the prior information from the rock physics to the seismic data inversion, which significantly improves the convergence. The inverted VTI model not only explains the reflection data (flattens the gathers), but also follows the basic geological and rock physics principles. The 3-D example in this chapter demonstrates that anisotropic WEMVA can further improve the subsurface model and further focus the subsurface image especially for the steeply dipping reflectors around the salt body.

ACKNOWLEDGEMENTS

The author thanks Schlumberger MultiClient for providing the field dataset. This paper includes data supplied by IHS Energy Log Services; Copyright (2013) IHS Energy Log Services Inc. I acknowledge the Stanford Center for Computational Earth and Environmental Science for providing computing resources.